BIOMIMETICS

Fly motion vision maximizes signal energy transfer between mechanical input and sensor output

J. Sean Humbert[1]*†, Holger G. Krapp[2]*†, James D. Baeder[3], Camli Badrya[4], Inés L. Dawson[5], Jiaqi V. Huang[2], Andrew Hyslop[3,6], Yong Su Jung[7], Alix Leroy[5], Cosima Lutkus[1], Beth Mortimer[5], Indira Nagesh[8], Clément Ruah[2], Simon M. Walker[9], Yingjie Yang[2], Rafal W. Żbikowski[10,11], Graham K. Taylor[5]*†

Insects achieve agile flight using a sensor-rich control architecture whose embodiment eliminates the need for complex computation. For example, their visual systems are tuned to detect the optic flow associated with specific self-motions, but what functional principle does this tuning embed, and how does it facilitate motor control? Here, we tested the hypothesis that evolution cotunes physics and physiology by aligning an insect's sensors to its dynamically important modes of self-motion. Specifically, we show that the spatial tuning of the blowfly motion vision system maximizes the open-loop Hankel singular values, which quantify the flow of signal energy from gust disturbances and control inputs to sensor outputs, jointly optimizing observability and controllability. This evolutionary principle differs from the conventional engineering-design paradigm of optimizing state estimation, with implications for robotic systems combining high performance with minimal actuator usage.

INTRODUCTION

Similar to fifth-generation fighter aircraft and small multirotors, flies and other insects are inherently unstable in flight. This makes them highly maneuverable but demands exquisite control. Technological and biological systems alike achieve this by combining information about motor input and sensor output (*1*) with an internal model of their dynamics (*2*), enabling them to observe and control their motion state in the face of disturbances. Whereas modern fly-by-wire control systems operate a computationally intensive control architecture with recursive state estimation and a small number of sensors and actuators, insects have evolved a computationally efficient control architecture with parallel processing and many sensors and actuators (*3*). For instance, the blowfly *Calliphora* fuses the output of ~10^5 sensory cells to provide information about its self-motion and uses at least 26 steering muscles to control its wingbeat, yet it weighs a mere 10^{-4} kg and consumes only 10^{-2} W of metabolic power in flight. The sensor-rich control architecture of insects may therefore point to a novel flight control paradigm in which specialized sensing avoids the need for generalized computation (*4*), but the underlying functional principle has yet to be identified (*5*).

One possibility is that an insect's sensors are tuned to produce signals that directly correspond to excitation of the natural modes of motion characterizing its flight dynamics (*3*). This principle, called the "mode-sensing hypothesis" (*3*, *5*), might serve to reduce computational complexity using embodied sensing. Under this hypothesis, an insect's sensors need only detect the characteristic patterns of self-motion that are excited by gust disturbances and control inputs (*6*) rather than provide a calibrated measurement of some general physical quantity such as angular velocity or airspeed (*3*). The mode-sensing hypothesis accords with the broader observation that biological sensors are exquisitely sensitive to change but poor at measuring absolutes (*3*), even varying their gain according to the behavioral state of the animal (*7*). It might also explain why the descending neurons that relay sensory information downstream to the flight motor fuse information from multiple sensory modalities because an insect's flight dynamics are characterized by coupled rotational and translational motions that stimulate multiple sensory systems simultaneously (*3*).

Here, we tested whether the mode-sensing hypothesis explains the tuning of the fly motion vision system, which is currently the best-understood example of a deep neural network in nature (*8*–*10*). Visually oriented animals, including flies, detect the wide-field optic flow stimuli experienced during self-motion by correlating local changes in luminance across neighboring photoreceptors before pooling this information globally. In flies, this operation is implemented by an array of elementary movement detectors whose responses are pooled by the lobula plate tangential cells (LPTCs) that form the output layer of the motion vision pathway. The LPTCs' response characteristics are best known for *Calliphora* (*11*), functioning as matched filters (*12*–*14*) tuned to detect specific patterns of optic flow associated with particular combinations of rotational and translational self-motion (*15*, *16*). Any global tuning principle relating to the fly's self-motion must therefore be embedded in the synaptic distribution and weighting of the dendritic inputs to its LPTCs, which are the level of the network at which information is pooled from across the optical array.

Each LPTC is tuned to detect some specific combination of rotation and translation defining a preferred direction of self-motion, which the mode-sensing hypothesis predicts should correspond to one or more dynamically relevant directions in the insect's state space (*3*). In principle, this hypothesis can be tested by analyzing a suitable model of the insect's flight dynamics (*5*), but no such model

[1]Department of Mechanical Engineering, University of Colorado, Boulder, CO, USA. [2]Department of Bioengineering, Imperial College London, London, UK. [3]Department of Aerospace Engineering, University of Maryland, College Park, MD, USA. [4]Department of Mechanical and Aerospace Engineering, University of California, Davis, CA, USA. [5]Department of Biology, University of Oxford, Oxford, UK. [6]European Space Agency, Noordwijk, Netherlands. [7]Department of Aerospace Engineering, Pusan National University, Busan, South Korea. [8]European Space Agency, Oxfordshire, UK. [9]School of Biomedical Sciences, University of Leeds, Leeds, UK. [10]School of Aerospace, Transport and Manufacturing, Cranfield University, Cranfield, Bedford, UK. [11]Spirent Communications PLC, Origin One, Crawley, West Sussex, UK.
*Corresponding author. Email: sean.humbert@colorado.edu (J.S.H.); h.g.krapp@imperial.ac.uk (H.G.K.); graham.taylor@biology.ox.ac.uk (G.K.T.)
†These authors contributed equally to this work.

has yet been elaborated for *Calliphora*. Moreover, although rigid-body flight dynamics models (*17*) have been successfully developed for several other insect species (*18*), they do not usually attempt to model the output of the insect's sensory system and do not accurately capture the detailed changes in wing kinematics involved in its flight control. Likewise, although recent neuromechanical models of insects are expressly designed to model the sensorimotor control of their behavior in a lifelike fashion (*19*, *20*), few have yet attempted to model flight in a biomechanically accurate manner (*21*). Even then, as simulation models, these neuromechanical models are not designed to enable the abstraction of control-theoretic principles, as is our aim here.

Our approach is to capture the dynamic mapping from mechanical input to sensor output analytically, which we achieved by creating a state-space model of blowfly flight dynamics and control. Subsequently, the most dynamically relevant directions in the insect's state space were identified, which we accomplished by analyzing the state-space model using control-theoretic tools called Gramians. Last, we tested whether the preferred self-motions of the LPTCs correspond to these dynamically relevant directions more closely than expected by chance. On the basis of the strong correspondences that we identify, we conclude that blowfly motion vision is tuned to maximize the transfer of signal energy from control inputs and gust disturbances to sensor outputs via the system state (Fig. 1). This end-to-end tuning principle optimizes the observability of the system state jointly with its controllability and disturbance sensitivity, which differs from the conventional engineering-design paradigm of placing sensors so as to optimize state estimation by maximizing observability alone (*22*, *23*). The evolutionary principle that we identify of tuning sensors to optimize observability jointly with controllability and disturbance sensitivity has important applications to the design of vehicles and robotic systems combining high performance with reduced computational overheads and minimal actuator usage (*24*).

RESULTS

Modeling approach

The simplest possible state-space model (Fig. 1) describing the dynamic mapping from mechanical input to sensor output linearizes an insect's six degrees of freedom of rigid-body motion about some equilibrium flight condition (*17*) to yield the linear time-invariant equations

$$\text{state equation: } \dot{\mathbf{x}}(t) = \mathbf{A}\mathbf{x}(t) + \mathbf{B}\mathbf{u}(t) + \mathbf{G}\mathbf{d}(t) \tag{1}$$

$$\text{output equation: } \mathbf{y}(t) = \mathbf{C}\mathbf{x}(t) \tag{2}$$

Here, all the forces and moments are assumed to be represented by their wingbeat averages, which is reasonable if the characteristic

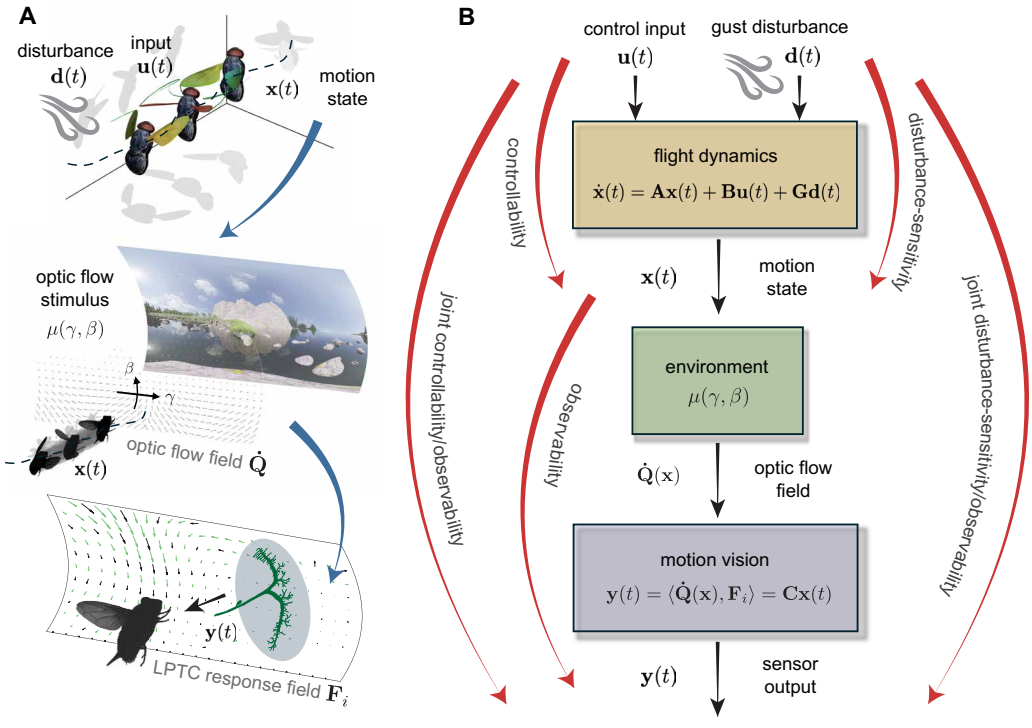

Fig. 1. Signal energy transfer in insect flight. (**A**) Blue arrows: Control inputs **u**(*t*) and gust disturbances **d**(*t*) produce changes in the insect's motion state **x**(*t*) described by the differential equations characterizing its flight dynamics. This self-motion generates sensory stimuli including an optic flow field through interaction with the local nearness μ(γ, β) of the environment. The output layer of the blowfly motion vision system comprises a set of LPTCs, each of which is matched to detect an optic flow field associated with a specific self-motion, yielding a sensor output **y**(*t*) related to the animal's motion state **x**(*t*). (**B**) Red arrows: Signal energy from control inputs and gust disturbances is stored in the system state, so the system's controllability and disturbance sensitivity are increased by maximizing signal energy storage. Stored signal energy is released through the evolution of the system state and retrieved at the sensor outputs, so the system's observability is increased by maximizing signal energy retrieval. A system that balances signal energy storage/retrieval jointly maximizes observability and controllability or disturbance sensitivity and thereby maximizes the flow of signal energy from control inputs or gust disturbances to sensor outputs via the system state.

timescales of any unstable or oscillatory modes of motion are at least an order of magnitude longer than the wingbeat (*17*). This assumption is true of other flies (*18*), and we validate it directly here for *Calliphora* having first parameterized the model.

The state equation (Eq. 1) models the insect's flight mechanics and is parameterized by the system matrix **A** characterizing the insect's natural response to perturbations in its motion state **x**. The control matrix **B** and disturbance matrix **G** characterize the insect's forced response to control inputs **u** and aerodynamic disturbances **d**, respectively. The output equation (Eq. 2) models how the resulting self-motions map to the insect's sensor output and is parameterized by the output matrix **C** characterizing the physiological mapping from the insect's motion state **x** to its sensor outputs **y**. Together, these two matrix equations describe the transfer of signal energy from control inputs and disturbances to sensor outputs via the system state (Fig. 1). Simplified versions of the state equation have been parameterized for a few other species (*18*), but these have not been coupled to an output equation modeling the resulting sensory output, and they have not been founded on an accurate model of the kinematic inputs used in flight control. Given our model's centrality to the conclusions that follow, we detail how we parameterize Eq. 2 empirically in relation to a blowfly's visual physiology and flight physics. We then analyze this model using control-theoretic methods to identify the functional principle that the tuning of the blowfly's motion vision system embodies.

Visual physiology

We first characterize the motion vision system whose tuning we aim to explain, providing the reader with a brief description of its anatomy and physiology, before using new and published electrophysiological recordings to parameterize the output equation (Eq. 2).

Visual output vector

The output layer of the fly motion vision system is formed by a set of wide-field optic flow–sensitive neurons called the LPTCs. A subset of the LPTCs in *Calliphora* is tuned to respond specifically to self-motion stimuli, including the 10 vertical system (VS) cells {VS1 to VS10} and three horizontal system (HS) cells {HSN, HSS, HSE} of each optic lobe (*11*, *15*, *25*, *26*). The VS and HS cells arborize ipsilaterally, yet some of their response fields extend across both visual hemispheres (Fig. 2B), which is important for distinguishing rotational from translational self-motion (*3*). This binocularity is made possible by a complex coupling arrangement (fig. S6) in which heterolateral LPTCs called V cells {V1, V2, V*x*} and H cells {H1, H2, H*x*} relay output from the contralateral optic lobe (*11*, *26*, *27*). The binocular VS and HS cell outputs are ultimately combined with output from other sensory modalities involved in flight control by descending neurons that relay sensory information to the wing, leg, and neck motor systems (*28*, *29*). Hence, whereas the VS and HS cells form the output layer of each optic lobe, the heterolateral V and H cells form a shallow hidden layer that is critical to the function of this bilaterally symmetric deep neural network (fig. S6). To allow us to analyze their respective functions, we used the characteristic responses of all 19 cells in each of the two mirror-symmetric optic lobes to form the 38 elements of the output vector **y**. To enable modeling the output vector **y**, we must quantify the LPTC responses using a combination of new and existing electrophysiological recordings, as described in the next section.

Electrophysiological measurements

Characterization of the LPTCs' electrophysiological responses to local image motion (Fig. 2, B to E) reveals that each cell's response field [i.e., the vector field describing its local motion sensitivity (LMS) and local preferred directions (LPDs)] resembles a coherent optic flow stimulus associated with some specific combination of rotational and translational self-motion (*16*). For example, it is well known that the VS cells signal combinations of heave translation and roll or pitch rotation (Fig. 2F) (*15*, *25*), whereas the HS cells signal combinations of yaw rotation and sideslip or forward translation (*26*). The responses of the heterolateral LPTCs have been less well studied, so to complete our model of the blowfly motion vision system, we characterized the V1, V2, and V*x* response fields of male and female flies experimentally (Fig. 2, C to E). We did so by making extracellular recordings of the cells' activity in response to local image motion, which we used to determine the spatial distribution of their LPDs and LMS across the visual field (see Materials and Methods). These new data from both sexes complement and complete existing recordings made extracellularly from the V and H cells (*26*, *30*, *31*) and intracellularly from the VS, HS, and H*x* cells of females only (*15*, *25*–*27*). Our results show no functional differences between males and females and demonstrate that the preferred rotation axes of V1, V2, and V*x* (Fig. 2G) each coincide with different subsets of the VS cells (Fig. 2F; see also fig. S6). The correspondence between the response fields of the LPTCs and the optic flow fields associated with specific combinations of rotational and translational self-motion is notable, but the dynamical importance of these patterns has only been examined qualitatively to date (*3*).

Physiological modeling of the output equation

The response fields $\{\mathbf{F}_i\}$ of the $i = 1, \ldots, 38$ LPTCs of the left and right optic lobes are defined in retinal azimuth and elevation coordinates $\{\gamma, \beta\}$ whose equatorial plane $\beta = 0$ is assumed to be held horizontal at equilibrium. The retinal coordinate system is assumed to rotate with the body such that the ray defining its origin coincides with the x axis used in our flight dynamics modeling (Fig. 3). This approximation is valid for the small perturbations that we model and is reasonable to the extent that compensatory head movements are driven optokinetically (*32*, *33*), supported by mechanosensory mechanisms including the fast gyroscopic haltere system (*29*). However, even the fastest haltere-induced response would not fully compensate for body rotations to maintain a level gaze during the initial phase of the perturbation (*34*). The magnitude of the optic flow experienced during translational self-motion varies inversely with distance to the visual environment. To determine how the LPTCs are expected to respond to rigid-body motion, we assume that the insect is flying at the centre of a 2-m cube, although we relax this assumption later. To parameterize the output equation (Eq. 2) in this environment, we compute the partial derivative of the optic flow field $\dot{\mathbf{Q}}$ with respect to each element of the state vector **x** (see Materials and Methods). We then take the inner products of the resulting matrices with the LPTC response fields $\{\mathbf{F}_i\}$ and use these to form the elements of the unilateral output matrix $\mathbf{C}'$, whose 38 normalized rows $\mathbf{c}'_i$ describe the preferred directions of self-motion of the 19 mirror-symmetric pairs of LPTCs. We treat the outputs of the left and right optic lobes separately (table S7). Last, because symmetric and asymmetric motions can be treated separately in our linearized flight dynamics model (see Fig. 3F), we restructure $\mathbf{C}'$ to form a bilateral output matrix **C** whose 38 normalized rows represent the summed and differenced responses of the 19 mirror-symmetric

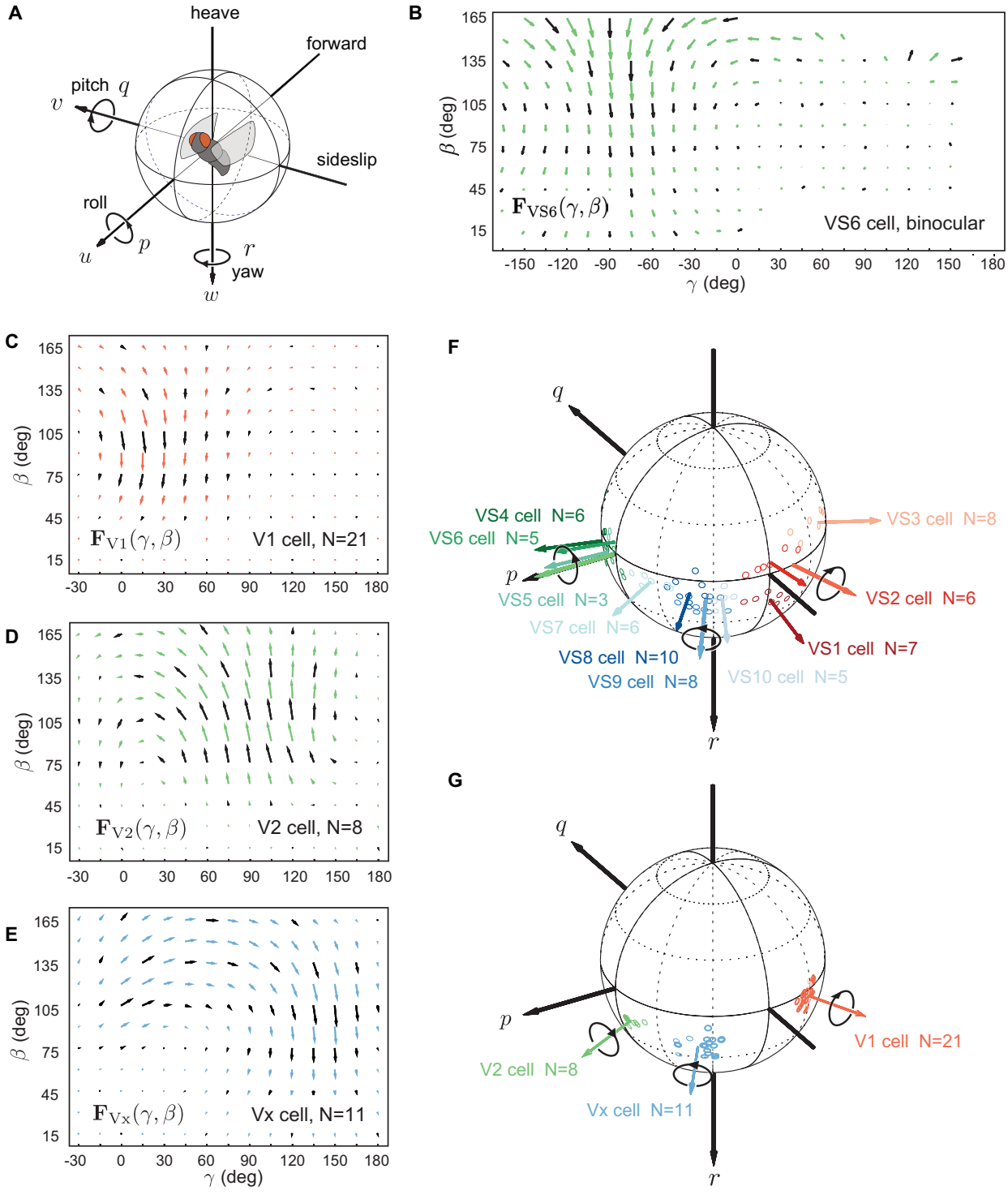

Fig. 2. The fly motion vision system. (**A**) A flying insect has six degrees of freedom in rotation {*p*, *q*, *r*} and translation {*u*, *v*, *w*}. Its compound eyes sense self-motion using an array of repeated elementary motion detectors whose outputs are pooled by the LPTCs. LPTCs build an output layer of 13 pairs of VS and HS cells connected by a hidden layer of at least six pairs of V and H cells coupling the left and right optic lobes. (**B**) Binocular response field of the left VS6 cell showing the neurons' LPDs and LMSs as a function of azimuth (γ) and elevation (β) in retinal coordinates. This closely resembles the optic flow associated with left-handed roll motion (*27*), and because the LPTCs only arborize ipsilaterally, the weak contralateral response visible here must be due to coupling by the heterolateral V cells. (**C** to **E**) Newly measured response fields of the right V cells, where *N* denotes the number of individuals from which the recordings were pooled. (**F** and **G**) Preferred rotation axes of the left VS (*15*, *25*) and V cells (new data); cells of the right optic lobe have responses that are mirror symmetric to those of the left optic lobe. Long arrows in (F) and (G) give the average preferred rotation axis of the functional groups VS1 to VS3, VS4 to VS7, and VS8 to VS10 and the spiking V1, V2, and V*x* cells, respectively. Black circular arrows indicate preferences for clockwise or counterclockwise rotations.

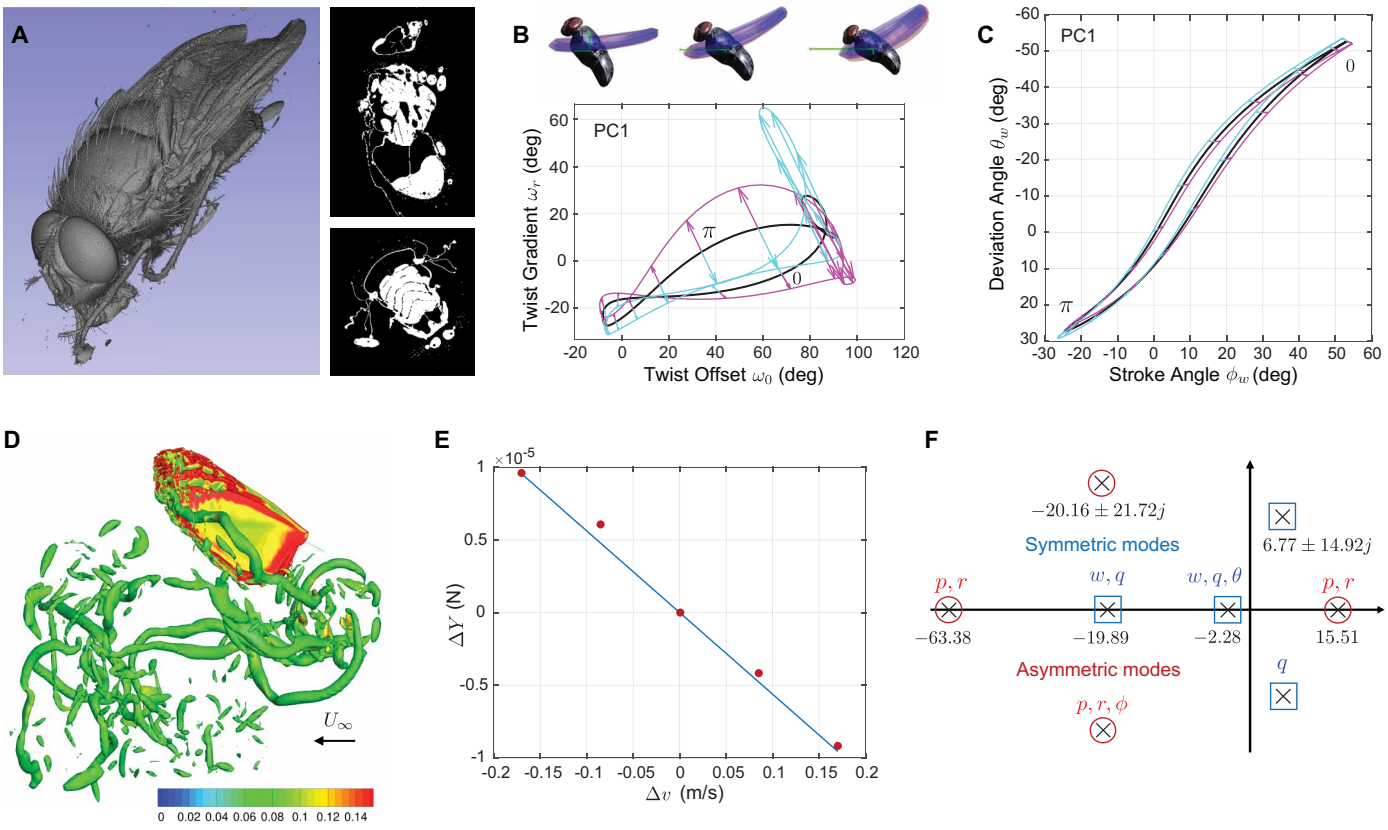

Fig. 3. Modeling of blowfly flight physics. (**A**) We estimated the fly's inertia tensor using synchrotron-based x-ray microtomography: Images show a three-dimensional rendering and longitudinal and transverse slices of a male blowfly. (**B** and **C**) We used high-speed videography to record the wing kinematics of free-flying blowflies over a range of flight speeds and used functional PC analysis to define a set of control inputs summarizing the coupled variation in wing-twist (B) and tip (C) kinematics: Phase portraits illustrate the reference wing kinematics (black) ± 1 SD (cyan/magenta) in the first principal component (PC1). PC1 involves coupled changes in stroke plane, stroke amplitude, and wing twist, which we may conceptualize as characterizing the result of the fly's limit-cycle control of its wingbeat oscillation (*70*). (**D**) We used a RANS solver to model how the aerodynamics vary with the kinematics; this image of the wing and wake shows vortex shedding at the end of the downstroke, visualized using iso-*Q* criterion surfaces ($Q = 0.001$) colored by vorticity. (**E**) We estimated the fly's stability and control derivatives by regressing the wingbeat-averaged aerodynamic forces and moments on the perturbed states or control inputs for a single wing; change in lateral force with respect to the change in lateral velocity is shown; control derivatives were estimated similarly by modeling the changes in the aerodynamic forces with respect to each modeled control input. (**F**) Eigenstructure of the system matrix **A** with labels denoting the dominant components of self-motion for the associated eigenvectors; note the pair of unstable modes with positive real parts, indicating that the fly's flight dynamics are inherently unstable.

pairs of LPTCs (see Fig. 4A below). This pairwise approach to combining the output of the left and right optic lobes is intended to reflect that each LPTC pair carries separable information about symmetric versus asymmetric motions and makes no explicit assumptions about the actual downstream connections of the LPTCs. This is necessary because our knowledge of how the descending neurons combine this information remains incomplete (*35*–*37*).

Flight physics

The parameterized output equation (Eq. 2) models how the insect's six degrees of freedom of rigid-body motion are represented in the 38-dimensional output of its motion vision system. To understand how this sensor output responds to control inputs and aerodynamic disturbances, we must also model the insect's flight dynamics by parameterizing the state equation (Eq. 1). Previous state-space models of insect flight control (*18*) have not attempted to identify the detailed control inputs that are available to the insect, so building a biologically meaningful model requires the development of new analytical modeling approaches, as described in the sections below.

State and disturbance vector

The insect's rigid-body flight dynamics (Fig. 2A) are described by the Newton-Euler equations of motion relating its linear and angular acceleration to the gravitational and aerodynamic forces and moments (*17*). For convenience, these vector quantities are defined in body-fixed stability axes whose x axis is aligned to the flight velocity vector at equilibrium and whose y axis is normal to the insect's symmetry plane. It follows that the insect's state vector $\mathbf{x}$ must contain complete information about its linear velocity $\mathbf{v} = [u\ v\ w]^T$ and angular velocity $\boldsymbol{\omega} = [p\ q\ r]^T$ with respect to an inertial reference frame, together with information about the roll and pitch angles of the body $\{\phi, \theta\}$, which is needed to keep track of gravity as the insect rotates. For the linearized system in Eq. 2, these eight elements of the state vector $\mathbf{x}$ are treated as small perturbations (δ) from level symmetric rectilinear flight at equilibrium and are separated into their symmetric and asymmetric parts $\mathbf{x}_{\text{long}} = [\delta u\ \delta w\ \delta q\ \delta\theta]^T$ and

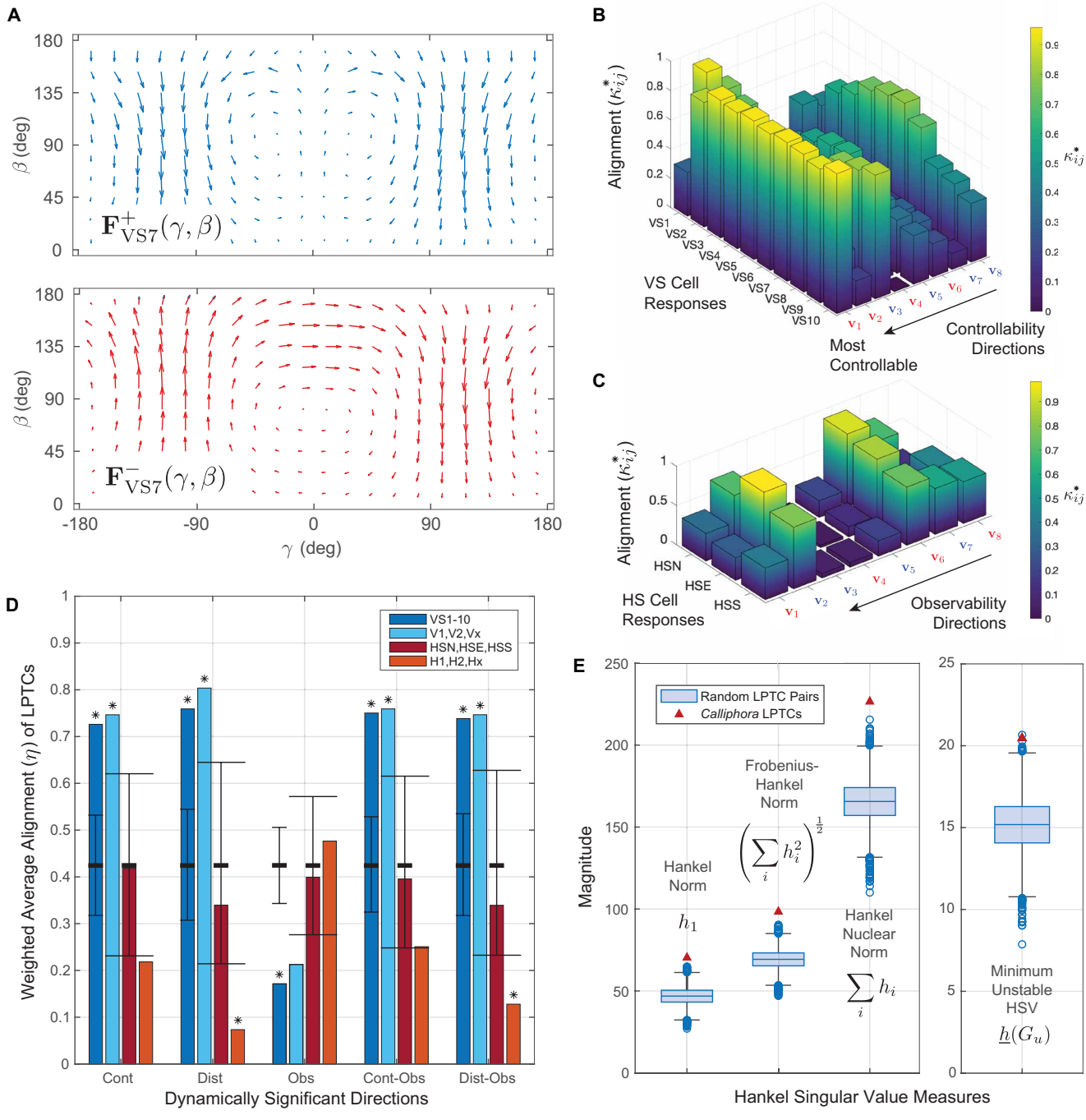

Fig. 4. Functional principles of blowfly sensorimotor design. (**A**) Each LPTC pair carries separable information about symmetric versus asymmetric motion, which we illustrate by taking the sum (blue) or difference (red) of their response fields, shown here for VS7. (**B** and **C**) The response fields shown in (A) encode the cells' preferred directions of rotational and translational self-motion, which the mode-sensing hypothesis predicts will be aligned to dynamically important directions in the insect's state space. To test this, we quantified their alignment to the ordered symmetric (blue) or asymmetric (red) eigenvectors of the controllability and observability Gramians $\{\mathbf{v}_1, \ldots, \mathbf{v}_8\}$, ranked by their dynamical significance (data in tables S8 and S9). Collectively, the VS cells strongly encode all of the most controllable directions of symmetric and asymmetric motion, whereas the HS cells strongly encode only the most observable direction of symmetric motion. (**D**) Averaging over each LPTC subpopulation, the V and VS cells strongly encode the directions that maximize controllability or disturbance sensitivity both independently and jointly with observability; asterisks (*) denote statistical significance controlling the overall type I error at $\alpha = 0.05$. No LPTC subpopulation is aligned to the most observable directions of motion, as would be conventional in engineering design. (**E**) To assess overall system performance, we computed four measures (the Hankel, Frobenius-Hankel and Hankel Nuclear norm, and the minimum unstable) of the HSVs $\{h_1, \ldots, h_8\}$ characterizing signal energy flow through the system for all 19 LPTC pairs (red points) and compared these with the HSVs of 10,000 randomly generated sets of preferred directions (blue box plot; whiskers extend ± 2.7 SD). The blowfly's HSVs are far higher than expected by chance, demonstrating that the LPTCs' tuning maximizes signal energy flow through the system. The first HSV provides an upper bound on signal energy flow from input to output.

$\mathbf{x}_{\text{lat}} = \left[\delta v\ \delta p\ \delta\phi\ \delta r\right]^T$, describing longitudinal and lateral motions, respectively. Bulk motion of the surrounding air mass produces the same relative airflow as translational or rotational self-motion, so we use analogous perturbation quantities to form the aerodynamic disturbances in the disturbance vector **d**.

Reference wing kinematics

A blowfly's wingbeat is a complex three-dimensional limit cycle motion involving substantial aeroelastic deformation, driven by muscular forces applied at the wing root through one of the most complex linkages in the natural world (*38*). To capture this complexity, we used four high-speed video cameras to record the deforming wing kinematics of $N = 28$ individuals over 274 flights at 3800 frames per second (fps) and used a voxel carving method (*39*) to identify the three-dimensional outline of the wings and estimate the pose of the body (Fig. 3B); see Materials and Methods. We measured the angular position of the wing tips (θ_w, ϕ_w) in a body-fixed coordinate system (Fig. 3C) and estimated the torsional deformation of the wings under a linear twist distribution for the pitch angle of the wing, $\omega[r] = \omega_0 + \omega_r r$ (Fig. 3B). We then fitted a Fourier series with a linear trend to each of the 2708 wingbeats that we recorded for either wing. We defined a set of reference wing kinematics for our aerodynamic modeling by averaging the Fourier coefficients over three wingbeats representing near-equilibrium flight. These three wingbeats were centered on the wingbeat that most nearly achieved level flight from within the subset of wingbeats associated with near-zero body acceleration ($<0.5\ \text{m s}^{-2}$). For generality, we set the reference wingbeat frequency ($f_e = 166$ Hz), reference flight speed ($u_e = 0.85\ \text{m s}^{-1}$), and reference body pitch angle ($\theta_e = 30°$) to their mean values over all of the wingbeats we measured and used these to model a reference condition of level forward flight.

Control input vector

Whereas the control inputs of an aircraft are known by design and include simple mechanical quantities such as throttle settings and control surface deflection angles, insect wings are passive structures that lack discrete control surfaces. This makes it challenging to identify what inputs an insect's control vector **u** should contain, but defining this in a biologically meaningful way is essential to any meaningful analysis of controllability. We therefore used functional principal components (PCs) analysis (*40*) to summarize the empirical variation in the Fourier coefficients describing each of the 2708 wingbeats that we had measured. This analysis decomposed the observed aeroelastic variation in the wing kinematics into a set of PCs characterizing the dominant kinematic couplings (Fig. 3, B and C; see Materials and Methods). The first four PCs define an orthonormal basis for the control vector **u** that is sufficient to capture 61% of the measured variation in the Fourier coefficients. We assumed that the four PCs could be controlled independently on each wing and used them together with the wingbeat frequency f to define the nine elements of the control vector **u**. It is an open question whether this approach is sufficient to describe all of the important kinematic variation in blowfly flight control, but our use of these four PCs is a pragmatic choice to ensure that the dimension of the resulting control input vector **u** is the same as that of the state vector **x**, resulting in a fully actuated, rather than under- or overactuated, system. Furthermore, in a qualitative sense, the first four PCs already capture the key kinematic control inputs that are known to be important in insect flight control (*41*), including coupled changes in stroke amplitude and stroke plane (Fig. 3C) and changes in the timing and extent of wing rotation at or around stroke reversal (Fig. 3B).

Physical modeling of the state equation

We used synchrotron-based x-ray microtomography (Fig. 3A) to estimate the inertia tensor of *Calliphora* for $N = 3$ freshly euthanized individuals and used a Reynolds-averaged Navier-Stokes (RANS) solver (Fig. 3D) to model the aerodynamic forces and moments acting at the wing hinge under the reference kinematics. Because the flight dynamics model is linearized about equilibrium, we adjusted the assumed body mass, body drag, and wing hinge moment arm so that the aerodynamic forces and moments balanced the gravitational force when integrated over the reference wingbeat kinematics. We then ran a computational experiment (*42*) in which we simulated the aerodynamic effect of small perturbations to the insect's motion state in **x**. These perturbations are aerodynamically equivalent to the gust disturbances in **d**, so having estimated the partial derivatives of the wingbeat-averaged aerodynamic forces and moments using a zero-intercept regression model (Fig. 3E), we were able to parameterize the system matrix **A** and disturbance matrix **G**. We parameterized the control matrix **B** in a similar manner for symmetric versus asymmetric control inputs, thereby completing our modeling of the state equation (Eq. 1).

Cotuning of physics and physiology

Having fully parameterized our state-space model of blowfly flight (Eq. 2), we had yet to identify the functional principle that underpins the physiological tuning of the LPTCs. We begin by examining the natural dynamics of the physical system as a prerequisite for the more advanced control-theoretic analyses that follow.

Eigenstructure of the flight dynamics

The system matrix **A** has an eigenstructure (Fig. 3F) similar to most other models of insect flight dynamics (*18*), describing a characteristic set of symmetric versus asymmetric, stable versus unstable, and oscillatory versus monotonic motions. We summarize these by reporting the nondimensional period ($\widehat{T}$) and/or time constant ($\widehat{\tau}$) of each mode expressed relative to the insect's wingbeat period. The symmetric modes are dominated by coupled pitch-heave motions, comprising a pair of fast ($\widehat{\tau} = 8.4$) and slow ($\widehat{\tau} = 72.9$) stable monotonic subsidence modes and a slow unstable oscillatory mode ($\widehat{T} = 70.0$; $\widehat{\tau} = 24.6$). The asymmetric modes are dominated by coupled roll-yaw motions, comprising a slow but heavily damped oscillatory mode ($\widehat{T} = 48.1$; $\widehat{\tau} = 8.2$), a fast stable monotonic subsidence mode ($\widehat{\tau} = 2.6$), and a fast unstable monotonic divergence mode ($\widehat{\tau} = 10.7$). The time constants of the unstable modes are large enough that the instability they describe will develop on a timescale of tens of wingbeats in the absence of closed-loop control. Given that the period of each oscillatory mode is also an order of magnitude longer than the wingbeat period, these results validate our earlier assumption that the aerodynamic forces and moments may be replaced by their wingbeat averages when modeling the rigid-body flight dynamics (Eq. 1). Moreover, because blowfly flight is inherently unstable with respect to both symmetric and asymmetric motions, it follows that the insect must use the output of its sensors to command closed-loop flight stabilization. That being so, how has evolution tuned the visual physiology of the blowfly in relation to its flight dynamics?

Formalization of the mode-sensing hypothesis

The tuning of the LPTCs is characterized by the normalized row vectors of the bilateral output matrix **C**, each of which represents a specific symmetric or asymmetic combination of optic-flow field (Fig. 4A) that the LPTCs are best tuned to detect (*5*). The mode-sensing hypothesis predicts that these physiologically preferred directions of self-motion should be matched to certain dynamically important directions of self-motion determined by the animal's flight dynamics (*3*). For the unstable system described by Eq. 2, those dynamically important directions are characterized by a set of real symmetric matrix structures called Gramians, which are defined in the frequency (ω) domain as

$$\text{Observability Gramian: } \mathbf{Y}_o = \frac{1}{2\pi}\int_{-\infty}^{\infty}\left(-j\omega\mathbf{I}-\mathbf{A}^T\right)^{-1}\mathbf{C}^T\mathbf{C}\left(j\omega\mathbf{I}-\mathbf{A}\right)^{-1}d\omega \tag{3}$$

$$\text{Controllability Gramian: } \mathbf{X}_c = \frac{1}{2\pi}\int_{-\infty}^{\infty}\left(j\omega\mathbf{I}-\mathbf{A}\right)^{-1}\mathbf{B}\mathbf{B}^T\left(-j\omega\mathbf{I}-\mathbf{A}^T\right)^{-1}d\omega \tag{4}$$

where **I** is the identity matrix (*43*). The disturbance-sensitivity Gramian $\mathbf{X}_d$ is composed similarly to the controllability Gramian $\mathbf{X}_c$, replacing **B** with **G**. These Gramians are evaluated as solutions to a combined pair of Riccati and Lyapunov equations (see the Supplementary Materials), but it is evident by inspection of Eq. 4 that they relate to the interaction between the natural response of the system described by the system matrix **A** and the output matrix **C**, the control matrix **B**, or the disturbance matrix **G**. Each Gramian therefore relates to one of the distinct flows of signal energy summarized by the red arrows in Fig. 1.

To explain their dynamical importance more formally, we note that the orthonormal eigenvectors $\{\hat{\mathbf{v}}_j\}$ and ordered eigenvalues $\{\lambda_j\}$ of each Gramian define the principal axes of an *n*-dimensional ellipsoid with semiaxis lengths $\sqrt{\lambda_j}$, the longest axes of which represent the most dynamically important directions in the insect's state space (*44*). For example, the eigenvectors and eigenvalues of the controllability Gramian $\mathbf{X}_c$ define the principal axes of the controllability ellipsoid $\mathcal{E}_c = \{\mathbf{x}\in\mathbb{R}^n; \mathbf{x}^T\mathbf{X}_c^{-1}\mathbf{x}\le 1\}$. The dynamical importance of this structure can be seen by noting that the controllability Gramian $\mathbf{X}_c$ is defined (*43*) such that the quantity $\|\mathbf{u}_{opt}\|^2 = \mathbf{x}_0{}^T\mathbf{X}_c^{-1}\mathbf{x}_0$ represents the minimum control input energy required to evolve the stable portion of the system to a given state $\mathbf{x}=\mathbf{x}_0$ and regulate the unstable portion of the system to the origin $\mathbf{x}=0$. It follows that the longest axes of the controllability ellipsoid $\mathcal{E}_c$ encode the most controllable directions in the insect's state space, representing the specific self-motions that can be produced with the least input energy $\|\mathbf{u}_{opt}\|^2$ at the controls.

The observability and disturbance-sensitivity ellipsoids are constructed similarly, such that the observability ellipsoid $\mathcal{E}_o$ encodes the most observable directions (i.e., the self-motions that characteristically yield the most output energy at the sensors), and the disturbance-sensitivity ellipsoid $\mathcal{E}_d$ encodes the most-sensitive directions (i.e., the self-motions that can be excited with the least input energy in a gust). These three ellipsoids thereby describe the specific self-motions that the insect is best able to drive $(\mathcal{E}_c)$, best equipped to estimate $(\mathcal{E}_o)$, and most prone to experience $(\mathcal{E}_d)$. Aligning the sensors to any of these sets of dynamically important directions would therefore reflect a different optimization principle associated with signal energy flow through the system (Fig. 1). Comparing these dynamically important directions with the preferred directions of the LPTCs (Fig. 4, B to D) allows a formal test of the mode-sensing hypothesis and the identification of any underlying optimality principles in the control-theoretic framework of observability, controllability, and disturbance sensitivity (*45*).

Directional tuning of the LPTCs

We quantified the alignment of the preferred directions of the LPTCs to the dynamically important directions of self-motion by taking their absolute inner products $\kappa_{ij} = \left|\left\langle\hat{\mathbf{c}}_i, \hat{\mathbf{v}}_j\right\rangle\right|$. However, because the inner product of any symmetric-asymmetric pairing is identically zero, we use κ^*_{ij} to distinguish symmetric-symmetric or asymmetric-asymmetric pairings for which $\kappa^*_{ij}\in[0,1]$. This analysis shows that the differenced responses of the three V cells and VS2 to VS10 are very strongly aligned $\left(\kappa^*_{ij}\ge 0.9\right)$ with the most controllable direction of asymmetric motion, whereas the differenced response of VS1 is similarly strongly aligned with the second-most controllable direction of asymmetric motion (Fig. 4B and table S8). Likewise, the summed responses of the subset {V1, V*x*, VS1, and VS2, VS8 to VS10} are strongly aligned $\left(\kappa^*_{ij}\ge 0.7\right)$ with the most controllable direction of symmetric motion (Fig. 4D). The same holds true for the disturbance-sensitivity directions, but the summed and differenced responses of the VS cells are only weakly aligned with the most observable directions of symmetric and asymmetric motion $\left(\kappa^*_{ij}\le 0.5\right)$. In contrast, the summed responses of the HS and H cells are all strongly aligned $\left(\kappa^*_{ij}\ge 0.7\right)$ with the most observable direction of symmetric motion (Fig. 4C and table S9), with those of the subset {HSE, H1, H2, H*x*} being especially so $\left(\kappa^*_{ij}>0.9\right)$.

Overall tuning of LPTC subpopulations

To assess the tuning of each subpopulation of LPTCs to each set of dynamically important directions, we defined their weighted mean alignment (η) as

$$\eta = \frac{\sum_{i=1}^{2n}\sum_{j=1}^{8}k_{ij}\sqrt{\lambda_j}}{n\sum_{j=1}^{8}\sqrt{\lambda_j}} \tag{5}$$

which measures the extent to which the preferred direction vectors of an entire subpopulation of LPTCs encode the longest axes of a given ellipsoid and generalizes to the case where the preferred directions of the LPTCs used to calculate the $\{\kappa_{ij}\}$ are replaced with a mirrored set of randomized direction vectors drawn from a uniform distribution on the unit sphere in $\mathbb{R}^8$. A Monte Carlo analysis run over 100,000 such sets yields an expected weighted mean alignment of $\overline{\eta}=0.42$ under the null hypothesis. Applying a Bonferroni correction to control the type I error rate at $\alpha=0.05$ (Fig. 4D), we found that the VS cells encode the most controllable and most sensitive directions much more strongly than expected by chance ($\eta=0.73$ and $\eta=0.76$, respectively; two-tailed $P<0.0025$) and the most observable directions more weakly ($\eta=0.17$; two-tailed $P<0.0025$). The V cells display similar properties, also encoding the most controllable and most sensitive directions much more strongly than expected by chance ($\eta=0.75$ and $\eta=0.80$, respectively; two-tailed $P<0.0025$). In contrast, the HS cells do not encode any set of dynamically important directions any more strongly than expected by chance ($\eta\le 0.42$), and the H cells encode the most-sensitive directions much more weakly ($\eta=0.07$; two-tailed $P<0.0025$). It

follows that the VS and V cells are tuned to encode the effects of control inputs and gust disturbances, whereas the H cells are tuned to observe characteristics of the optic flow field that are comparatively insensitive to disturbances.

Joint optimization of sensing and control

The properties of controllability, observability, and disturbance sensitivity relate to signal energy flow to or from the system state and so depend on our choice of coordinate system for the state vector $\mathbf{x}$. That choice is meaningful for a technological system whose internal state is represented explicitly in its programming, but it is ambiguous for a biological system whose internal state cannot be directly observed. This ambiguity is eliminated by the alternative hypothesis that instead of being tuned to optimize any one such property in a given state space, the preferred directions of the LPTCs are matched to the directions of self-motion that jointly optimize controllability and observability or disturbance sensitivity and observability. A system that implemented this principle would be globally optimal in the sense that it would maximize the transfer of signal energy from input to output and hence distinctive in the sense that it would not depend on our choice of coordinate system for the state. For example, if evolution has tuned the VS cells to detect the effects of control inputs, then we should expect them to be strongly aligned to the joint most controllable and observable directions. Conversely, if evolution has tuned the HS cells to observe characteristics of the optic flow field that are robust to gust disturbances, then we should expect them to be weakly aligned to the joint most sensitive and observable directions.

The jointly optimized directions of self-motion are given by the normalized column vectors $\{\hat{\mathbf{t}}_j\}$ of the transformation matrix $\mathbf{T}^{-1}$, where $\breve{\mathbf{x}} = \mathbf{T}\mathbf{x}$ is a balancing transform that equalizes and simultaneously diagonalizes the transformed Gramians. Applying this balancing transform, which is distinct up to multiplication by a sign matrix, we have either $\breve{\mathbf{X}}_c = \breve{\mathbf{Y}}_o$ or $\breve{\mathbf{X}}_d = \breve{\mathbf{Y}}_o$, where $\breve{\mathbf{Y}}_o = \left(\mathbf{T}^{-1}\right)^T \mathbf{Y}_o \mathbf{T}^{-1}$ is a diagonal matrix. The diagonal entries of this matrix are the system's Hankel singular values (HSVs), which may be calculated directly as $h_j = \sqrt{\lambda_j}$ where $\{\lambda_j\}$ are the ordered eigenvalues of $\mathbf{Y}_o\mathbf{X}_c$ or $\mathbf{Y}_o\mathbf{X}_d$. The HSVs are similarity invariants that do not depend on the choice of coordinate system for $\mathbf{x}$, and they measure the degree of joint observability and controllability or disturbance sensitivity in the directions $\{\hat{\mathbf{t}}_j\}$ in the original coordinate system. Whereas the eigenvectors of the balanced Gramians in the new coordinates are orthogonal, the directions that they define in the original state space are not.

To assess the overall tuning of the LPTCs to these jointly optimized directions, we calculated their absolute inner products as $\kappa_{ij} = \left|\left\langle \hat{\mathbf{c}}_i, \hat{\mathbf{t}}_j \right\rangle\right|$, reporting their weighted mean η using the HSVs $h_j = \sqrt{\lambda_j}$ as the weights in Eq. 5. This analysis (Fig. 4D; see also Fig. 5, A and B, and tables S10 and S11) confirms that the VS and V cells encode the most controllable/observable ($\eta \geq 0.75$) and most sensitive/observable directions ($\eta \geq 0.74$) much more strongly than expected by chance (two-tailed $P < 0.0025$). The VS and V cells thereby embed the principle of encoding the directions in state space for which signal energy flow through the system is maximized. In other words, they are tuned to sense the modes of motion whose excitation yields the greatest sensor output for a given input of energy at the controls or in a gust. In contrast, the H cells encode the most sensitive/observable directions much more weakly than expected by chance ($\eta = 0.13$; two-tailed $P < 0.025$). In other words, they are tuned to be insensitive to the modes of motion that are most readily excited by aerodynamic disturbances.

A functional principle of visuomotor tuning

The preceding analyses compare the randomly generated directions or preferred directions of the LPTCs with the biological ground truth of the parameterized state-space model (Eq. 2). This approach enables us to draw conclusions about the directional tuning of the individual LPTCs, but it risks circular reasoning because their preferred directions also define the output matrix $\mathbf{C}$ that is used to generate the observability Gramian $\mathbf{Y}_o$ (Eq. 3). This circularity can be avoided together by composing a semirandom observability Gramian $\tilde{\mathbf{Y}}_o$ from the original system matrix $\mathbf{A}$ and a random output matrix $\tilde{\mathbf{C}}$ formed by generating 19 random direction vectors, mirroring these to yield 19 mirror-symmetric pairs, and taking their sums and differences to yield a bilateral output matrix with 38 rows. We then use $\tilde{\mathbf{Y}}_o$ to compute the randomized HSVs as $\tilde{h}_j = \sqrt{\lambda_j}$, where the $\{\lambda_j\}$ are the ordered eigenvalues of $\tilde{\mathbf{Y}}_o\mathbf{X}_c$ or $\tilde{\mathbf{Y}}_o\mathbf{X}_d$.

Figure 4E shows four measures of the HSVs associated with the fly's joint controllability and observability directions fall at the upper extreme of the null distribution of 10,000 randomly generated sets. The first measure is the Hankel norm for the open-loop system or the largest HSV h_1. The second is the Hankel-Frobenius norm, $\sqrt{\sum_i h_i^2}$, the third is the Hankel Nuclear norm, $\sum_i h_i$, and the fourth is the minimum HSV $\underline{h}(G_u)$ from the unstable partition G_u of the system. Of particular interest is the minimum unstable HSV, which has been shown to be directly related to the worst-case control energy and robustness to additive uncertainty in closed loop (*24, 46*). This confirms our conclusion that the preferred directions of the blowfly motion vision system are specifically adapted to maximize the flow of signal energy from control inputs to sensor outputs, where signal energy is defined for an arbitrary vector signal $\mathbf{w}(t)$ as

$$\text{signal energy: } \|\mathbf{w}(t)\|^2_{L_2[0,\infty)} = \int_0^\infty \|\mathbf{w}(t)\|_2^2 \, dt \qquad (6)$$

and $\|\cdot\|_2$ is the Euclidean vector norm. Moreover, the first HSV provides an upper bound on signal energy flow from input to output and is higher for the biological ground truth than for any of the randomly generated systems in Fig. 4E. Similar conclusions hold for the fly's joint disturbance-sensitivity and observability directions and hence for the flow of signal energy from gust disturbances to sensor outputs (fig. S5, B and D). Last, given that the neck motor neurons that drive optokinetic head movements display response properties similar to those of the VS and HS cells (*32*), we infer that the same principle of maximizing signal energy transfer is also likely to apply at the level of the neck motor system driving any compensatory head movements.

Robustness of conclusions

To avoid making any assumptions on how the LPTC outputs are combined, we verified that the same conclusions hold when the HSVs are calculated for the unilateral output matrix $\mathbf{C}'$ as opposed to the bilateral output matrix $\mathbf{C}$ (fig. S5). We also tested how the assumed nearness distribution of the visual environment influences the fly's HSVs by synthesizing 100 perturbed output matrices and observability Gramians with respect to two different environmental configurations: a cuboid environment generated by perturbing the 2-m cube used in the analyses above and a segmented ellipsoid

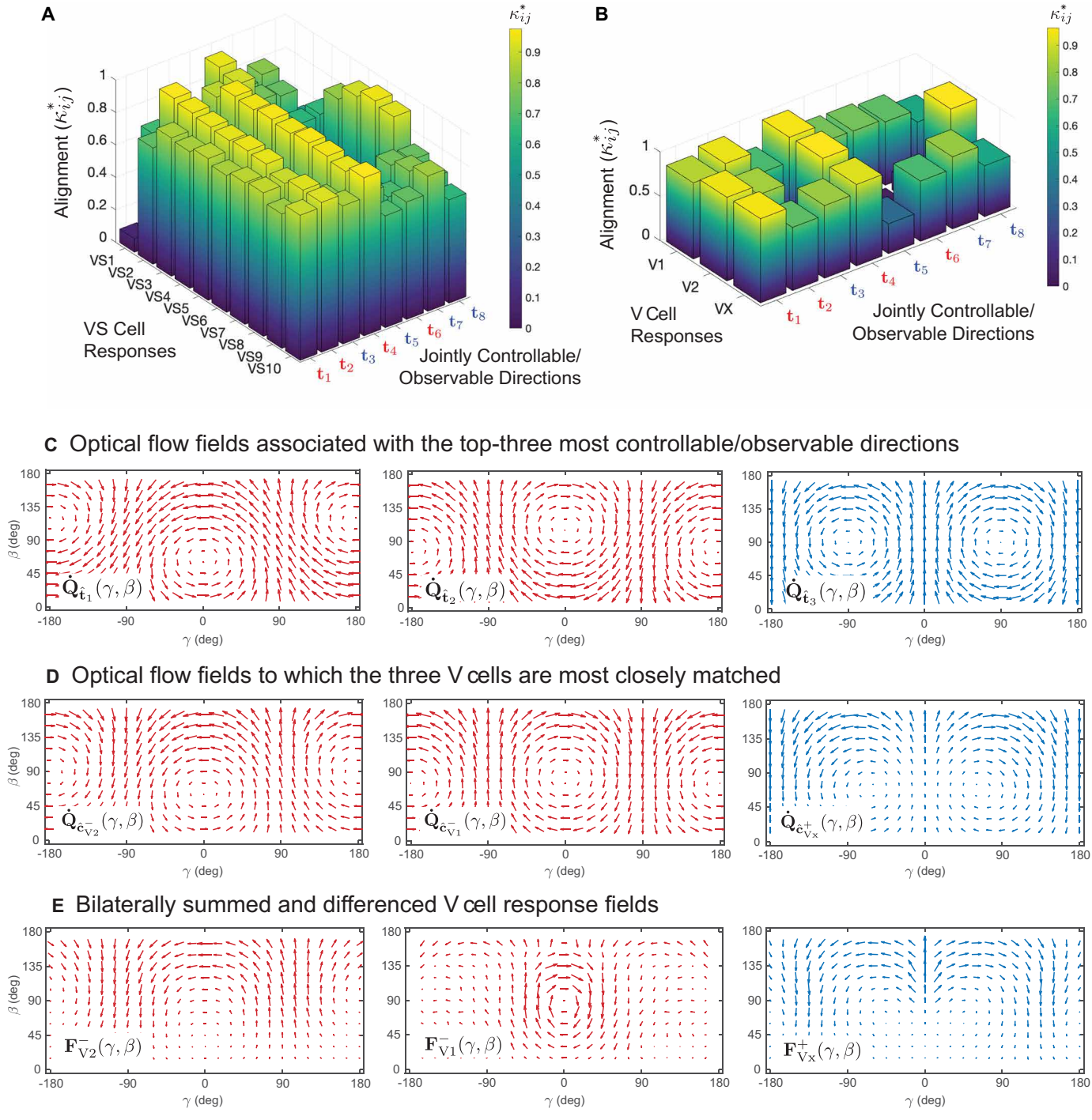

Fig. 5. Tuning of the VS LPTCs to the fly's jointly controllable/observable directions of self-motion. (**A** and **B**) Signal energy flow is maximized when a system's sensors are matched to its most controllable/observable directions of self-motion. To demonstrate the closeness of this tuning in the blowfly, we first quantified the alignment of the preferred directions of the LPTCs to the ordered symmetric (blue) or asymmetric (red) column vectors $\{\mathbf{t}_1, \ldots, \mathbf{t}_8\}$ of the inverse balancing transformation matrix. These vectors span the entire controllable/observable subspace of the insect, and the bilaterally summed and differenced response fields of the VS and V cell pairs are shown to be strongly aligned with all of them (data in tables S10 and S11). (**C** and **D**) To demonstrate this visually, we also computed the reprojected optic flow fields corresponding to (C) the top three most controllable/observable directions of symmetric (blue) or asymmetric (red) self-motion and (D) the preferred directions of symmetric (blue) or asymmetric (red) self-motion for the three V cell pairs. (**E**) The summed and differenced response fields of the V cell pairs also resemble the reprojected optic flow fields corresponding to the joint most controllable/observable directions of motion, with spatial variation due to the embedded nearness distribution corresponding to a natural environment (*16*).

environment generated by perturbing a sphere of equal nominal volume (fig. S4, A and C). The parameters defining each configuration were selected at random from a uniform distribution with 50% variation from their nominal values to generate variability and asymmetry in the assumed visual environment. The resulting distributions of perturbed HSVs again remain at the extreme upper end of the null distribution (fig. S4, B and D). We conclude that the directional tuning of the LPTCs maximizes signal energy transfer between the inputs and outputs of the system as opposed to maximizing conventional design criteria such as the accuracy of state estimation.

DISCUSSION

How does the LPTCs' tuning embed the functional principle of maximizing signal energy transfer from input to output? As we have shown (Fig. 4), the VS LPTCs are strongly aligned to the insect's most controllable/observable directions of self-motion. Furthermore, their alignment is high not only for all eight of the joint controllability/observability directions but also for those that are the most controllable/observable (Fig. 5, A and B). Specifically, every one of the joint controllability/observability directions is strongly aligned ($\kappa^*_{i,j} \geq 0.75$) with at least one VS cell and at least one V cell (Fig. 5, A and B), and the same result holds true for the joint disturbance-sensitivity/observability directions. In contrast, the HS cells encode the joint controllability/observability directions much less strongly (Fig. 4D), effectively encoding a region of state space that is of lesser dynamical importance to the insect and that is likely to be of greater importance in guidance and navigation tasks.

How is this combination of breadth and specificity possible? In principle, the 10 pairs of VS cells have sufficient redundancy to encode any set of eight directions strongly, but the same cannot be said of the three pairs of V cells. The strength of the V cells' alignment to all of the joint controllability/observability directions instead reflects the fact that these eight directions are highly nonorthogonal, describing a narrow region of the insect's state space that is dominated by the same rotational motions that dominate the VS and V cell responses (Fig. 2, B to E). Specifically, the natural modes of motion of a blowfly (Fig. 3F) are dominated by pitch-heave and roll-yaw dynamics (table S6), which are the same self-motions that the VS LPTCs are tuned to sense. This is the region of state space that is of the greatest dynamical importance to the insect, and the hidden layer of V cells embeds it in its entirety (Fig. 5B).

The strength of this embedding can be visualized by comparing the summed and differenced response fields of the V cells (Fig. 5E) with the optic flow fields corresponding to their preferred directions of self-motion (Fig. 5D) and with the optic flow fields corresponding to the top three most controllable/observable directions for the insect (Fig. 5C). The closeness of the match is notable, and this together with the broader correspondence between the VS LPTCs and the joint controllability/observability and disturbance-sensitivity/observability directions makes the VS and V cells well suited to modulating flight stabilization and control. In contrast, the HS LPTC responses are dominated by forward motion and yaw sideslip. With the exception of yaw, these motions are of lesser dynamical importance, but they include the equilibrium forward-flight condition about which the dynamics are linearized. It follows that the HS cells are better suited to encoding steady-state properties of the insect's self-motion associated with its navigational state and guidance behaviors, which are also the directions of self-motion that are most robust to disturbance.

What are the functional benefits of structuring a system in this way? Intuitively, it makes sense to optimize a system's sensors in relation to the endogenous inputs and exogenous disturbances that excite its motion, but how does this work in the context of closed-loop control? Multi-input multi-output (MIMO) systems are inherently directional; not only does the amplitude of the input or disturbance signal determine the magnitude of the response but the directionality can also have an influence. The transfer of signal energy from input to output is maximized by optimizing the storage and retrieval of signal energy to and from the system state. Hence, applying the principle of maximizing the HSVs by tuning the sensing directions in **C** to the actuation directions of **B** through the natural modes of **A** balances the open-loop system so that it is optimized for maximum achievable closed-loop performance, which is manifest in several ways. First, it maximizes the open-loop gain of the plant G so that the resulting outputs will have increased signal magnitude, improving the open-loop signal-to-noise ratio. A similar result is not achievable by simply increasing the gain of the controller K because the measurements (and attendant noise) will be amplified simultaneously. Second, we note that the minimum unstable HSV $\underline{h}(G_u)$ (Fig. 4E) is inversely proportional to the worst-case actuator effort $\|KS_o\|_\infty$ over any controller K (*46*)

$$\min_K \|KS_o\|_\infty = \frac{1}{\underline{h}(G_u)} \tag{7}$$

where the sensitivity function $S_o = (I + GK)^{-1}$ is the closed-loop map between exogenous inputs such as disturbances **d**, noise, and references to the internal error signal **e** for the standard negative feedback loop. Therefore, increases in the minimum unstable HSV will result in a reduction in the input demand and control energy required to stabilize an unstable system. Last, the norm $\|KS_o\|_\infty$ is inversely proportional to the size of the additive perturbation that the resulting closed-loop system can tolerate (*47*); therefore, tuning the open-loop system in this way maximizes the achievable robustness to unstructured additive uncertainty over all possible controllers (*24*). In addition, the approach of tuning an open-loop system to maximize potential closed-loop performance, independent of the feedback architecture, is well documented and has precedent in the sensor placement and selection literature (*48*).

The evolutionary principle that we have identified of maximizing signal energy transfer from motor input to sensor output represents a radical departure from the design of current technological systems. In conventional engineering practice, sensor placement is usually optimized at a late stage of platform design and typically aims to maximize the accuracy of state estimation. This is achieved by maximizing the signal-to-noise ratio at the sensors, which means placing them to optimize observability (*23, 49*). Tuning the LPTC response fields in this manner would yield sensor outputs with the best possible signal-to-noise ratio, but if the system was rarely excited in those directions by its own actions or by disturbances, then it would not be energetically efficient to encode them. In contrast, natural selection tends to produce neural architectures that prioritize energetic and hence computational efficiency (*50*), so it is reasonable to suppose that the principle of maximizing signal energy throughput might also extend to the sensorimotor systems of other organisms.

The sensorimotor pathway of the blowfly visuomotor system—in which thousands of directionally selective local inputs are integrated

on the dendrites of large-field motion-sensitive neurons (LPTCs) to form a convergent architecture—although not essential for encoding dynamically relevant state directions, represents one of several implementation choices available to a robotic designer. A conventional robotics approach would retain dense sensory measurements and fuse them through a recursive observer or Kalman filter, which offers well-established benefits in estimation accuracy and recovery of unmeasured states when sufficient computational resources and model fidelity are available (*51*). However, recursive estimators fundamentally rely on temporal averaging and internal dynamics, which necessarily introduce delay, require memory and initialization, and can reduce practical robustness in high-bandwidth or agile flight applications.

In contrast, sensorimotor convergence implements spatial weighting at the sensing stage, embedding dynamically relevant combinations of state variables directly in the sensor outputs. This enables instantaneous noise reduction through spatial summation without introducing estimator dynamics or detailed kinematic modeling and reduces communication, memory bandwidth, and implementation complexity. Although recursive estimation may yield superior performance under ideal computational conditions, convergence-based sensing offers a low-latency and hardware-efficient alternative that becomes particularly compelling in resource-constrained, edge, or microrobotic systems. From this perspective, the two approaches should be viewed as complementary architectural options rather than competing solutions, with the appropriate choice determined by application-specific constraints rather than estimation optimality alone.

As the field of robotics transitions from platforms with sensorimotor architectures composed of small numbers of discrete sensors and actuators to architectures with continuum sensing and actuation, new design principles will be required. To achieve optimal performance, synthesis approaches that simultaneously consider the specification of sensors, actuators, and platform dynamics will be critical. Embodied design principles that have produced nature's most effective and agile organisms (*52*), such as the joint maximization of signal energy storage and retrieval uncovered here, have the potential to revolutionize the early-stage design process and maximize the performance of future engineering systems. These bioinformed design principles will prove especially relevant in applications that, similar to living organisms, are resource constrained by computational capacity and power or energy density and are inherently MIMO systems where directionality of exogenous inputs is important.

MATERIALS AND METHODS

Electrophysiological characterization of LPTC response fields

Animals and dissection method

Adult male and female blowflies (*Calliphora vicina*) were taken from a laboratory colony at Imperial College London, where they were kept on a 12:12-hour light:dark cycle. Flies were dissected following a standardized procedure (*53*): After removing the legs, proboscis, and wings, the resulting wounds were sealed with beeswax before the animal was fixed to a dedicated holder, with the thorax tilted 45° down relative to the head. The rear head capsule was opened using a microscalpel, and fat tissue, air sacs, and some tracheae were removed to enable placement of extracellular electrodes in the lobula plate. Saline solution (*54*) was added to keep the neural tissue moist. The center of the head was positioned at the center of a goniometric visual stimulation device and aligned using the symmetrical deep pseudopupil method (*55*) at a precision of ±1° in head roll, pitch, and yaw. Because blowflies are invertebrates, no ethical approvals are required for experimental work.

Extracellular recording and visual stimulation method

We used extracellular tungsten electrodes with 3-megohm impedance (FHC Inc., Bowdoin, ME, USA; product code: UEWSHGSE3N1M) to record the neural activity of the V1, V2, and V*x* heterolateral LPTCs. The electrodes were placed in different target areas depending on the recorded cell type using the tracheal branching patterns of the lobula plate as landmarks. Neuronal signals were amplified using a custom-built differential amplifier with a nominal gain of 10,000, sampled and digitized at 20 kHz using a NI DAQ board (USB-6211), and stored on the hard drive of a PC. Response fields were characterized only when the signal-to-noise ratio between recorded LPTC spikes and background noise was greater than 2:1, in which case a simple threshold-based method was sufficient to reliably detect time-stamped spikes of the recorded cell (fig. S1).

We used a custom-built automated goniometric recording platform to present a moving visual stimulus at any specified azimuth (γ) and elevation (β) in the fly's retinal coordinates. A liquid crystal display monitor (AOC AGON AG251FZ) was placed 0.3 m in front of the animal, running at a refresh rate of 240 Hz. We presented square-wave visual gratings (minimum and maximum intensity: 0.28 and 265.70 cd m^{-2}; Michelson contrast: 0.9979) moving perpendicular to their orientation typically at 1- or 3-Hz temporal frequency behind a circular aperture subtending 24°. Experiments where different temporal frequencies between 0.3 and 3 Hz were applied did not affect the self-motion preferences of the cells. To assess a cell's LPD and LMS, the grating was moved in eight different directions at a spacing of 45°. Each motion stimulus was presented for 1 s, followed by a brief period of 0.5 s during which a homogeneous screen was presented at the mean luminance level. In total, the motion stimulus was presented at 84 positions over both eyes, covering the nearly 4π visual field of the fly.

LPDs and LMSs

At any given stimulus position, we calculated the vector sum from the responses to the eight different stimulus directions. Magnitude and direction of the resulting vector were taken to indicate the LMS and LPD, respectively. Those response parameters were plotted as a function of azimuth (γ) and elevation (β) in a cylindrical projection of the fly's spherical visual field to reveal the recorded cell's global response field properties (Fig. 2, B to E). In each response field, all vectors were normalized to the maximum response measured. To facilitate recognition of the global response field organization, the measured data in Fig. 2 (B to E; black vectors) are complemented by interpolated data (colored vectors). The data collected using this method are in line with those previously gathered using a local stimulus that changed its motion direction continuously (*32, 53, 54*). Although we presented the motion stimulus at 84 positions over both eyes, the response fields plotted for the heterolateral LPTCs in Fig. 2 (C to E) show only the data obtained upon visual stimulation within the visual hemisphere that results in the highest motion sensitivity (i.e., strongest directional-selective response), which is typically the visual hemisphere ipsilateral to the dendritic input region of the recorded cell.

Modeling of LPTC response properties

Preferred self-motion parameters

We estimated each cell's preferred self-motion parameters using an iterative least-squares algorithm (KvD) proposed by Koenderink and van Doorn (*56*). The KvD algorithm is applied to retrieve the rotation, $\boldsymbol{R}$, and the translation, $\boldsymbol{T}$, of a self-motion inducing an optic flow field that best fits the global response field organization of the studied cell. Hence, if we consider a given LPTC to act as a matched filter for optic flow (*16*), the KvD algorithm enables us to estimate which self-motion components of a moving fly would most strongly stimulate the cell. We applied a slightly modified version of the KvD algorithm in which we assumed a homogeneous distance distribution to obtain the preferred rotation axes of the V1, V2, and V*x* cells (Fig. 2G); the preferred rotation axes of the VS cells (Fig. 2F) were computed using a similar method by Krapp *et al.* (*25*). There were no meaningful sex differences in the preferred rotation axes of the three heterolateral LPTCs, and we therefore pooled the response field data across sexes.

Encoding of motion state by the LPTCs

The matched filter hypothesis proposed in (*16*) suggests that each LPTC's output can be considered as a comparison between the cell's response field and the optic flow fields generated during the animal's self-motion, where each cell is tuned to sense a specific flow field and hence some specific combination of rotational and translational self-motion. Mathematically, this comparison can be modeled as an inner product on a discrete (*16, 57, 58*) or continuous (*59–61*) spatial domain. Here, we define a spatial inner product between the instantaneous pattern of optic flow $\dot{\mathbf{Q}}$ and a given tangential cell's response field $\mathbf{F}_i$ as

$$\mathbf{y}_i = \left\langle \dot{\mathbf{Q}}, \mathbf{F}_i \right\rangle = \int_{S^2} \dot{\mathbf{Q}} \cdot \mathbf{F}_i \, d\Omega, i = 1, \ldots, m \tag{8}$$

where m is the number of LPTC response fields under consideration. The details of the optic flow pattern $\dot{\mathbf{Q}}$ can be found in the Supplementary Materials.

Formulation of the output matrix

For a given set of unilateral response fields $\{\mathbf{F}_i\}$, the collection of LPTC outputs forms a nonlinear output equation $\mathbf{y} = \mathbf{h}(\mathbf{x})$. To characterize the rigid body state information encoded by the selected set of measured response fields, each output is linearized about the reference flight equilibrium $\bar{\mathbf{x}}$. The resulting matrix entries in the unilateral output equation $\mathbf{y} = \mathbf{C}'\mathbf{x}$ (Eq. 2) are given by

$$\mathbf{C}'_{ij} = \left.\frac{\partial h_i}{\partial x_j}\right|_{\bar{\mathbf{x}}} = \left.\frac{\partial \left\langle \dot{\mathbf{Q}}, \mathbf{F}_i \right\rangle}{\partial x_j}\right|_{\bar{\mathbf{x}}} = \left.\left\langle \frac{\partial \dot{\mathbf{Q}}}{\partial x_j}, \mathbf{F}_i \right\rangle\right|_{\bar{\mathbf{x}}} \tag{9}$$

In this form, each row of the associated $\mathbf{C}'$ matrix represents the state information present in the signal from a specific LPTC response field, that is, the direction it encodes in state space. To develop the output matrix for the measured set of 19 left and right LPTC cell response fields, the raw data were first converted into stability frame coordinates according to the axis definitions of fig. S2A. $(\gamma, \beta) = (0°, 90°)$ in the plotted response fields (Figs. 2, B to E, and 4A) corresponds to the ray line along the $\hat{\boldsymbol{x}}_b$ axis in fig. S2B. The recorded LPD and LMS distributions in the response fields were smoothed with a two-dimensional Gaussian filter and then approximated with up to 8° spherical harmonics in the azimuth and elevation directions to facilitate an accurate numerical spatial integration.

For our baseline calculation, an enclosed rectangular prism environment (fig. S4A) was assumed with scaling parameters (g_N, g_S, a_E, a_W, h_D, and h_U) all set to a distance of 1 m, and as before, the reference flight condition was set to the mean forward flight speed of $u_s = 0.8509$ m s^{-1} that we measured (see below), such that $\bar{\mathbf{x}} = \begin{bmatrix} u_s & w_s & q_s & \theta_s & v_s & p_s & \phi_s & r_s \end{bmatrix}^T = [0.08509\ 0\ 0\ 0\ 0\ 0\ 0\ 0]^T$ in the stability axes. The corresponding patterns of partial derivatives of the optic flow $\partial \dot{\mathbf{Q}} / \partial x_i$ were computed by systematically perturbing each of the rigid body states and taking finite differences.

The results were used to compute the inner products numerically, resulting in the estimated response field state encoding shown in table S7. To perform the subsequent analysis, we extract the entries according to the rigid body state vector from the flight dynamics model formulation, $\mathbf{x} = \begin{bmatrix} \delta u_s & \delta w_s & \delta q_s & \delta\theta_s & \delta v_s & \delta p_s & \delta\phi_s & \delta r_s \end{bmatrix}^T$. The states $\{\delta x_s, \delta y_s, \delta z_s, \delta\psi_s\}$ typically are not included in the linearized dynamics because a homogeneous atmosphere assumption is used. In the resulting matrix $\mathbf{C}_{ij}'$, consecutive odd and even indices $\{i = 1, \ldots, 38\}$ correspond to the left and right cells of an LPTC pair. Last, because the flight dynamics model (Eq. 1) splits into symmetric and asymmetric parts, we form the 38 normalized rows $\hat{\mathbf{c}}_i$ of the bilateral output matrix $\mathbf{C}$ (Eq. 2) by summing or subtracting the responses of the $k = 1, \ldots, 19$ mirror-symmetric pairs of LPTCs such that $\hat{\mathbf{c}}_k^+ = \left(\mathbf{c}'_{2k} + \mathbf{c}'_{2k-1}\right) / \left\|\mathbf{c}'_{2k} + \mathbf{c}'_{2k-1}\right\|$ and $\hat{\mathbf{c}}_k^- = \left(\mathbf{c}'_{2k} - \mathbf{c}'_{2k-1}\right) / \left\|\mathbf{c}'_{2k} - \mathbf{c}'_{2k-1}\right\|$, as shown in Fig. 4A.

Reprojected optic flow fields

Any given direction of self-motion will produce a specific optic flow field in a given visual environment. We reprojected the optic flow fields $\dot{\mathbf{Q}}_{\hat{\mathbf{c}}_i}(\gamma, \beta)$ and $\dot{\mathbf{Q}}_{\hat{\mathbf{t}}_i}(\gamma, \beta)$ corresponding to the specific self-motion directions $\mathbf{x} = \hat{\mathbf{c}}_i$ or $\mathbf{x} = \hat{\mathbf{t}}_i$ in state space (Fig. 5, C to E) by substituting the expressions of the vectors $\omega = \begin{bmatrix} p & q & r \end{bmatrix}^T$, $\mathbf{v} = [u\ \ v\ \ w]^T$, and $\mathbf{r} = \begin{bmatrix} \cos\gamma \sin\beta & \sin\gamma \sin\beta & \cos\beta \end{bmatrix}^T$ in the stability frame $\mathcal{S}$, along with an analytical expression for the nearness of the environment $\mu(\gamma, \beta, \mathbf{q})$ into the representation for $\dot{\mathbf{Q}}$ above. The resulting azimuth γ and elevation β components (fig. S2) of $\dot{\mathbf{Q}}$ are given by

$$\begin{aligned} \dot{\mathbf{Q}}_\gamma &= p\cos\beta\cos\gamma + q\cos\beta\sin\gamma - r\sin\beta + \mu(u\sin\gamma - v\cos\gamma) \\ \dot{\mathbf{Q}}_\beta &= p\sin\gamma - q\cos\gamma + \mu(-u\cos\beta\cos\gamma - v\cos\beta\sin\gamma + w\sin\beta) \end{aligned} \tag{10}$$

as plotted in Fig. 5 (C to E).

Measurement and modeling of free-flight kinematics

Animals and experimental protocol

Larval *C. vicina* were reared on red meat at 20°C until pupation; the adult flies were fed on a combination of milk powder formula and mashed banana and were flown from 2 to 3 days posteclosion. Individuals were allowed to fly freely within a 1-m-diameter opaque acrylic sphere with diffuse overhead lighting. The interior of the sphere was decorated with pieces of card to provide visual contrast, and an ultraviolet light was placed at the top to stimulate loitering flight maneuvers. High-speed video sequences were captured using four synchronized Photron SA3 cameras (Photron Ltd., West Wycombe, UK) with 180-mm macro lenses (Sigma Imaging Ltd., Welwyn Garden City, UK), viewing the insect through clear portholes in the upper hemisphere and recording at 3800 fps and 768 by 640 pixels. Backlighting was provided by four infrared light-emitting diode (LED) lights (Dragon1IR PowerStars LED, Intelligent LED Solutions, Thatcham, UK) operating at wavelengths well beyond the visible

spectrum of the insect (*62*) (centroid wavelength: 850 nm; spectral bandwidth at 50% intensity: 30-nm full width at half maximum). Recordings were triggered because the insect passed through the center of the sphere, capturing forward flight punctuated by fast saccadic maneuvers. In total, we recorded $N = 2708$ wingbeats from 205 maneuvering flights made by 28 individual blowflies, involving a broad range of wing kinematics including symmetric and asymmetric variation in stroke amplitude, stroke plane angle, and wing twist.

Kinematic reconstruction

The cameras were calibrated using a nonlinear least-squares bundle adjustment routine (*63*) in MATLAB (MathWorks Inc., Natick, MA), using images of a calibration grid presented in a wide range of positions and orientations. For the main analysis, we used background subtraction and automatic thresholding to segment the pixels and used a shape-carving method to identify the set of voxels containing the wings and body (*39*). We reprojected the wing voxels as a mask for tracing the outline of the wing in each frame and used the shape-carving algorithm on this linear feature to reconstruct the leading and trailing edges in three dimensions. We used the major axis of the body voxels to define the insect's x axis and the line connecting the wing roots to define the insect's transverse y axis. We constructed a right-handed body axis system in which to measure the kinematics of the right wing and a left-handed body axis system in which to measure the kinematics of the left wing. These were measured by defining an extrinsic y-x-z rotation sequence bringing the x axis of a set of rotating axes initially aligned with the body axes into alignment with the wing chord connecting the trailing edge to the leading edge at some given spanwise position (r). The local pitch angle of the wing (ω) is defined as the first angle in this rotation sequence and was measured at six evenly spaced spanwise stations on the interval $r \in [0.3, 0.8]$, where r is expressed as a proportion of wing length. We summarized the instantaneous spanwise variation in ω by fitting the regression model $\omega[r] = \omega_0 + \omega_r r + \epsilon[r]$, where $\epsilon[r]$ is a Gaussian error term. We call ω_0 the twist offset and ω_r the twist gradient. The deviation angle θ_w and stroke angle ϕ_w represent the second and third angles in the extrinsic y-x-z rotation sequence and describe the elevation and azimuth of the wingtip in a set of body axes originating at the wing root. It follows that the insect's wing kinematics are measured by estimating $\phi_w[t]$, $\theta_w[t]$, $\omega_0[t]$, and $\omega_r[t]$ for the right and left wings separately at every sample time t.

Fourier series representations of wing kinematics

For each flight sequence, we fitted quintic smoothing splines modeling $\phi_w[t]$, $\theta_w[t]$, $\omega_0[t]$, and $\omega_r[t]$ for each wing as analytical functions of continuous time t. The spline tolerance that we used for each kinematic variable was chosen to preserve information up to the third harmonic of wingbeat frequency for ϕ_w and θ_w and up to the fifth harmonic for ω_0 and ω_r. We then used a piecewise linear transform to map continuous time t onto wingbeat phase $\varphi(t)$ by taking the turning point of the summed angular velocity of both wingtips in the stroke plane to define $\varphi = 0$ as the start of the downstroke. Last, we evaluated the splines at 101 evenly spaced phases of each wingbeat on the interval $\varphi \in [0, 2\pi]$ so that all wingbeats were directly comparable despite variability in the wingbeat period. Fitting each wingbeat separately, we used multiple regression with time-linear and time-periodic predictor variables to model the four primary kinematic variables $\phi_w[\varphi]$, $\theta_w[\varphi]$, $\omega_0[\varphi]$, and $\omega_r[\varphi]$ as detrended Fourier series of the form

$$h[\varphi] = K_L(\varphi - \pi) + K_0 + \sum_{k=1}^{P} \left(K_{2k-1}\cos(k\varphi) + K_{2k}\sin(k\varphi)\right) + \epsilon[\varphi] \quad (11)$$

where $\epsilon[\varphi]$ is a Gaussian error term and K_L and $K_0 \ldots K_{2P}$ are fitted coefficients. The time-linear coefficient K_L accounts for the fact that any actual wingbeat cycle is unlikely to begin and end in exactly the same kinematic state and multiplies $(\varphi - \pi)$ rather than φ so that this term has zero mean over the wingbeat cycle. The Fourier coefficients $K_0 \ldots K_{2P}$ are fitted with $P = 3$ for ϕ_w and θ_w, and with $P = 5$ for ω_0 and ω_r, to capture all of the harmonic content preserved by the quintic smoothing splines.

Functional PC analysis

Collecting the Fourier coefficients for a single wingbeat together as $\mathbf{K}^{\phi_w} = \left[K_0^{\phi_w} \ldots K_{2P}^{\phi_w}\right]$ for the stroke angle ϕ_w, and similarly for the other primary kinematic variables, we may summarize the time-periodic variation for all N wingbeat pairs in the matrix

$$\mathbf{Z}_P = \begin{bmatrix} {}_1\mathbf{K}^{\phi_w} & {}_1\mathbf{K}^{\theta_w} & {}_1\mathbf{K}^{\omega_r} & {}_1\mathbf{K}^{\omega_0} \\ \vdots & \vdots & \vdots & \vdots \\ {}_{2N}\mathbf{K}^{\phi_w} & {}_{2N}\mathbf{K}^{\theta_w} & {}_{2N}\mathbf{K}^{\omega_r} & {}_{2N}\mathbf{K}^{\omega_0} \end{bmatrix} \quad (12)$$

We used functional PC analysis to decompose this matrix into a new set of time-periodic basis functions characterizing the key kinematic couplings available for flight control. This was implemented by subtracting the column means from the matrix of Fourier coefficients $\mathbf{Z}_P$ to yield the centered matrix $\mathbf{Z} = \mathbf{Z}_P - \overline{\mathbf{Z}}_P$ and computing its singular value decomposition

$$\mathbf{Z} = \mathbf{U}\mathbf{\Sigma}\mathbf{V}^T \quad (13)$$

where $\mathbf{\Sigma}$ is a diagonal matrix containing the singular values of $\mathbf{Z}$, which are the positive square roots of the eigenvalues of $\mathbf{Z}^T\mathbf{Z}$ arranged in descending order. The columns of V contain the right-singular vectors of $\mathbf{Z}$, which are the eigenvectors of $\mathbf{Z}^T\mathbf{Z}$, normalized such that $\mathbf{V}^T\mathbf{V} = \mathbf{I}$. Because $\mathbf{Z}^T\mathbf{Z}$ is a scalar multiple of the covariance matrix of $\mathbf{Z}$, the orthonormal basis V that its eigenvectors define is aligned with the principal directions of the kinematic variation between wingbeats. Because each row of the PC matrix $\mathbf{V}$ corresponds to one of the Fourier coefficients, each of its columns defines a distinct time-periodic kinematic coupling, which we refer to as PC1, PC2, etc. (fig. S7).

Aerodynamic modeling of stability and control derivatives

Computational fluid dynamics modeling

We performed three-dimensional RANS simulations of the aerodynamics of the right wing of *Calliphora* using the OVERTURNS solver (*64*–*66*). We simulated a reference condition of level symmetric forward flight with a freestream velocity of $U_\infty = 0.8509\ \mathrm{m\ s^{-1}}$ and a wingbeat frequency of $f = 166.188$ Hz, corresponding to the mean values measured for these variables over the 2708 wingbeats whose kinematics we had recorded (see above). We used a mean body pitch angle $\theta_e = 30.365°$ and defined a set of reference wing kinematics by taking the mean of $\mathbf{Z}_P$ over three consecutive wingbeats centered on the wingbeat most nearly achieving level flight among the subset of

wingbeats for which the body acceleration was near zero (<0.5 m s^{-2}). We assumed a pure laminar boundary layer based on the measured mean chord length of 2.7 mm and chord Reynolds number of 1746. We used 720 time steps per wingbeat cycle with 12 subiterations, which allowed us to capture the unsteady flow characteristics with reasonable computational time. Tables S2 and S3 summarize the simulation parameters and input setup. The dimensions of the structured wing mesh were 195 (chordwise), 201 (spanwise), and 76 (wall-normal), and the initial wall normal spacing was 1×10^{-5} mean chord. Combined with the background mesh, this gave a total of 1.12×10^{7} node points.

Computational experiments

We perturbed the reference kinematics to simulate the aerodynamic effect of control inputs and small perturbations to the motion state of the body. We used the three components of translational velocity $\{u, v, w\}$ and angular velocity $\{p, q, r\}$ referred to the body axes $\mathcal{B}$ as the perturbed states and used the wingbeat frequency f together with PC1 to PC4 of the time-periodic wingbeat kinematics as control perturbations. Among the six perturbed state variables $\{u, v, w, p, q, r\}$, the perturbation level was set at ±10 and ±20% of freestream velocity U_∞ for the three flight velocities $\{u, v, w\}$ and at ±2.5 and ±5% of wingbeat frequency f for the three angular rates $\{p, q, r\}$. Among the five control variables, we perturbed PC1 to PC4 by ±0.5 and ±1.0 SDs and perturbed the wingbeat frequency f by ±1.5 and ±3%, corresponding to ±2.5 and ±5.0 Hz, respectively. We computed the three components of aerodynamic force $\{X, Y, Z\}$ and moment $\{L, M, N\}$ referred to the body axes $\mathcal{B}$ (fig. S3A). The time-averaged forces and moments had already converged reasonably by the start of the third wingbeat cycle, so we obtained their wingbeat-averaged values by taking the mean of the forces and moments over the third and fourth wingbeat cycles of each simulation.

Aerodynamic derivatives

To estimate the stability and control derivatives for our linearized flight dynamics model, we first subtracted the total aerodynamic forces and moments in each perturbed condition from those obtained in the reference flight condition and then fitted a zero-intercept linear regression through the origin to estimate the corresponding partial derivative of the aerodynamic forces and moments (Fig. 3B and fig. S3, D to F). The resulting aerodynamic derivatives are defined for the right wing using forces and moments resolved at the right wing hinge and were mirrored to model the aerodynamic forces and moments on the left wing under the equivalent kinematics. The results for the left and right wings were then combined to estimate the stability derivatives (table S4) and control derivatives (table S5) resolved at the center of mass, in a model enforcing equilibrium under the reference wing kinematics (see the Supplementary Materials for details). We used the unilateral control inputs to form sets of symmetric control inputs $\{u_0, u_1, u_2, u_3, u_4\}$ and asymmetric control inputs $\{u'_1, u'_2, u'_3, u'_4\}$ through symmetric changes in wingbeat frequency f and symmetric or asymmetric application of perturbations in PC1 to PC4.

Microtomographic estimation of inertia tensor

Animals and tomographic method

Two male and one female *C. vicina* from the Imperial College London colony were sealed in 0.5-ml Eppendorf tubes, having been fed and watered to satiation and then weighed. The tubes were placed individually in the TOMCAT beamline of the Swiss Light Source synchrotron facility and were irradiated at a 12-keV beam energy until the flies were dead and no further motion artifacts occurred. A 100-μm-thick, Ce-doped LuAG scintillator was placed at a distance of 272 mm behind the sample to convert the transmitted x-rays into visible light. The resulting image was magnified twofold using an Edge 5.5 Microscope, and 1501 projection images were collected at 60 ms of exposure time, whereas the sample was rotated through 180°. To image the entirety of each fly, it was necessary to image three overlapping volumes in this way. Phase retrieval was performed using the Paganin algorithm (*67*), setting the real and imaginary parts of the deviation from one of the complex refractive index of the material to 1×10^{-7} and 1×10^{-9}, respectively. Tomographic reconstruction was performed using a Fourier transform–based algorithm, resulting in voxels with an isotropic spacing of 3.25 μm.

Estimation of inertia tensor

We segmented the tomograms automatically, using thresholding and morphological operations to mask voxels corresponding to the cross section of the Eppendorf tube and any exterior voxels. The tomograms were then combined into one continuous stack across the three samples for each specimen, using unique cross-sectional features such as hairs to align the image stacks manually along their common longitudinal axis. The complete image stack was loaded into Fiji (*68*), and the BoneJ plugin (*69*) was used to calculate the mass moments of inertia about the principal axes of the specimen, assuming a uniform density of 1.1 g cm^{-3} appropriate to insect cuticle and muscle. The mass (m) estimates arrived at using this method (table S1) were identical to the weights taken at the start of the experiment to within the 0.01-g readability of the balance. Because the moments of inertia about the first and second principal axes were identical to within ±1% (table S1), we set $I_y = I_z$ for the purposes of the flight dynamics modeling and set I_x equal to the moment of inertia about the third principal axis. Assuming isometry, we nondimensionalized the moments of inertia by dividing through by $m^{5/3}$ and then rescaled these using the value of m assumed in the flight dynamics model.

Supplementary Materials

The PDF file includes:

Supplementary Text
Figs. S1 to S7
Tables S1 to S11
References (*71–86*)

Other Supplementary Material for this manuscript includes the following:

Data file S1

REFERENCES AND NOTES

1. W. P. Chan, F. Prete, M. H. Dickinson, Visual input to the efferent control system of a fly's "gyroscope". *Science* **280**, 289–292 (1998).
2. D. M. Wolpert, Z. Ghahramani, M. I. Jordan, An internal model for sensorimotor integration. *Science* **269**, 1880–1882 (1995).
3. G. K. Taylor, H. G. Krapp, "Sensory systems and flight stability: What do insects measure and why?" in *Insect Mechanics and Control*, vol. 34 of *Advances in Insect Physiology*, J. Casas, S. J. Simpson, Eds. (Academic Press, 2007), pp. 231–316.
4. R. Zbikowski, Sensor-rich feedback control: A new paradigm for flight control inspired by insect agility. *IEEE Instrum. Meas. Mag.* **7**, 19–26 (2004).
5. H. G. Krapp, G. K. Taylor, J. S. Humbert, "The mode-sensing hypothesis: Matching sensors, actuators and flight dynamics" in *Frontiers in Sensing* (Springer Vienna, 2012), pp. 101–114.
6. G. C. H. E. de Croon, J. J. G. Dupeyroux, C. De Wagter, A. Chatterjee, D. A. Olejnik, F. Ruffier, Accommodating unobservability to control flight attitude with optic flow. *Nature* **610**, 485–490 (2022).
7. G. Maimon, A. D. Straw, M. H. Dickinson, Active flight increases the gain of visual motion processing in *Drosophila*. *Nat. Neurosci.* **13**, 393–399 (2010).

8. S.-Y. Takemura, A. Bharioke, Z. Lu, A. Nern, S. Vitaladevuni, P. K. Rivlin, W. T. Katz, D. J. Olbris, S. M. Plaza, P. Winston, T. Zhao, J. A. Horne, R. D. Fetter, S. Takemura, K. Blazek, L.-A. Chang, O. Ogundeyi, M. A. Saunders, V. Shapiro, C. Sigmund, G. M. Rubin, L. K. Scheffer, I. A. Meinertzhagen, D. B. Chklovskii, A visual motion detection circuit suggested by *Drosophila* connectomics. *Nature* **500**, 175–181 (2013).
9. M. S. Maisak, J. Haag, G. Ammer, E. Serbe, M. Meier, A. Leonhardt, T. Schilling, A. Bahl, G. M. Rubin, A. Nern, B. J. Dickson, D. F. Reiff, E. Hopp, A. Borst, A directional tuning map of *Drosophila* elementary motion detectors. *Nature* **500**, 212–216 (2013).
10. J. K. Lappalainen, F. D. Tschopp, S. Prakhya, M. McGill, A. Nern, K. Shinomiya, S. Takemura, E. Gruntman, J. H. Macke, S. C. Turaga, Connectome-constrained deep mechanistic networks predict neural responses across the fly visual system at single-neuron resolution. bioRxiv 532232 [Preprint] (2023). https://doi.org/10.1101/2023.03.11.532232.
11. K. Hausen, Decoding of retinal image flow in insects. *Rev. Oculomot. Res.* **5**, 203–235 (1993).
12. R. Wehner, 'Matched filters' — Neural models of the external world. *J. Comp. Physiol.* **161**, 511–531 (1987).
13. D. C. O'Carroll, N. J. Bidwell, S. B. Laughlin, E. J. Warrant, Insect motion detectors matched to visual ecology. *Nature* **382**, 63–66 (1996).
14. E. J. Warrant, Sensory matched filters. *Curr. Biol.* **26**, R976–R980 (2016).
15. H. G. Krapp, R. Hengstenberg, Estimation of self-motion by optic flow processing in single visual interneurons. *Nature* **384**, 463–466 (1996).
16. M. O. Franz, H. G. Krapp, Wide-field, motion-sensitive neurons and matched filters for optic flow fields. *Biol. Cybern.* **83**, 185–197 (2000).
17. G. K. Taylor, A. L. R. Thomas, Dynamic flight stability in the desert locust *Schistocerca gregaria*. *J. Exp. Biol.* **206**, 2803–2829 (2003).
18. M. Sun, Insect flight dynamics: Stability and control. *Rev. Mod. Phys.* **86**, 615–646 (2014).
19. V. Lobato-Rios, S. T. Ramalingasetty, P. Gizem Özdil, J. Arreguit, A. J. Ijspeert, P. Ramdya, NeuroMechFly, a neuromechanical model of adult *Drosophila melanogaster*. *Nat. Methods* **19**, 620–627 (2022).
20. S. Wang-Chen, V. A. Stimpfling, T. K. C. Lam, P. G. Özdil, L. Genoud, F. Hurtak, P. Ramdya, NeuroMechFly v2: Simulating embodied sensorimotor control in adult *Drosophila*. *Nat. Methods* **21**, 2353–2362 (2024).
21. R. Vaxenburg, I. Siwanowicz, J. Merel, A. A. Robie, C. Morrow, G. Novati,Z. Stefanidi, G.-J. Both, G. M. Card, M. B. Reiser, M. M. Botvinick, Y. Tassa, S. C. Turaga, Whole-body simulation of realistic fruit fly locomotion with deep reinforcement learning. bioRxiv 584515 [Preprint] (2024). https://doi.org/10.1101/2024.03.11.584515.
22. D. Georges, "The use of observability and controllability Gramians or functions for optimal sensor and actuator location in finite-dimensional systems" in *Proceedings of 1995 34th IEEE Conference on Decision and Control* (IEEE, 1995), vol. 4, pp. 3319–3324.
23. B. Boyacioglu, M. Babaei, A. H Mamo, S. Bergbreiter, T. L. Daniel, K. A. Morgansen, "Sensor placement for flapping wing model using stochastic observability Gramians" in *2024 American Control Conference* (IEEE, 2023), pp. 4950–4966.
24. Z. Turin, G. K. Taylor, H. G. Krapp, E. Jensen, J. Sean Humbert, Matching sensing to actuation and dynamics in distributed sensorimotor architectures. *IEEE Access* **13**, 13584–13605 (2025).
25. H. G. Krapp, B. Hengstenberg, R. Hengstenberg, Dendritic structure and receptive-field organization of optic flow processing interneurons in the fly. *J. Neurophysiol.* **79**, 1902–1917 (1998).
26. H. G. Krapp, R. Hengstenberg, M. Egelhaaf, Binocular contributions to optic flow processing in the fly visual system. *J. Neurophysiol.* **85**, 724–734 (2001).
27. H. Krapp, "Repräsentation von Eigenbewegungen der Schmeißfliege *Calliphora erythrocephala* in VS-Neuronen des dritten visuellen Neuropils," thesis, Eberhard-Karls-Universität (1995).
28. N. Strausfeld, H. Seyan, J. Milde, The neck motor system of the fly *Calliphora erythrocephala*— I. Muscles and motor neurons. *J. Comp. Physiol. A* **160**, 205–224 (1987).
29. R. Hengstenberg, Gaze control in the blowfly *Calliphora*: A multisensory, two-stage integration process. *Semin. Neurosci.* **3**, 19–29 (1991).
30. K. Karmeier, H. G. Krapp, M. Egelhaaf, Robustness of the tuning of fly visual interneurons to rotatory optic flow. *J. Neurophysiol.* **90**, 1626–1634 (2003).
31. K. D. Longden, H. G. Krapp, State-dependent performance of optic-flow processing interneurons. *J. Neurophysiol.* **102**, 3606–3618 (2009).
32. S. J. Huston, H. G. Krapp, Visuomotor transformation in the fly gaze stabilization system. *PLOS Biol.* **6**, e173 (2008).
33. K. D. Longden, A. Schützenberger, B. J. Hardcastle, H. G. Krapp, Impact of walking speed and motion adaptation on optokinetic nystagmus-like head movements in the blowfly *Calliphora*. *Sci. Rep.* **12**, 11540 (2022).
34. B. J. Hardcastle, H. G. Krapp, Evolution of biological image stabilization. *Curr. Biol.* **26**, R1010–R1021 (2016).
35. W. Gronenberg, N. J. Strausfeld, Premotor descending neurons responding selectively to local visual stimuli in flies. *J. Comp. Neurol.* **316**, 87–103 (1992).
36. A. Wertz, A. Borst, J. Haag, Nonlinear integration of binocular optic flow by DNOVS2, a descending neuron of the fly. *J. Neurosci.* **28**, 3131–3140 (2008).
37. A. Wertz, B. Gaub, J. Plett, J. Haag, A. Borst, Robust coding of ego-motion in descending neurons of the fly. *J. Neurosci.* **29**, 14993–15000 (2009).
38. S. M. Walker, D. A. Schwyn, R. Mokso, M. Wicklein, T. Müller, M. Doube, M. Stampanoni, H. G. Krapp, G. K. Taylor, In vivo time-resolved microtomography reveals the mechanics of the blowfly flight motor. *PLOS Biol.* **12**, e1001823 (2014).
39. S. M. Walker, A. L. R. Thomas, G. K. Taylor, Operation of the alula as an indicator of gear change in hoverflies. *J. R. Soc. Interface* **9**, 1194–1207 (2012).
40. I. Nagesh, S. M. Walker, G. K. Taylor, Motor output and control input in flapping flight: A compact model of the deforming wing kinematics of manoeuvring hoverflies. *J. R. Soc. Interface* **16**, 20190435 (2019).
41. G. K. Taylor, Mechanics and aerodynamics of insect flight control. *Biol. Rev.* **76**, 449–471 (2001).
42. M. Sun, Y. Xiong, Dynamic flight stability of a hovering bumblebee. *J. Exp. Biol.* **208**, 447–459 (2005).
43. K. Zhou, G. Salomon, E. Wu, Balanced realization and model reduction for unstable systems. *Int. J. Robust Nonlinear Control* **9**, 183–198 (1999).
44. B. A. Moore, Principal component analysis in linear systems: Controllability, observability, and model reduction. *IEEE Trans. Automat. Contr.* **26**, 17–32 (1981).
45. R. W. Zbikowski, G. K. Taylor, "System-theoretic interpretation of the mode sensing hypothesis" (Tech. Rep. AFRL-AFOSR-UK-TR-2014-0036, Air Force Research Laboratory, 2014).
46. K. Glover, Robust stabilization of linear multivariable systems: Relations to approximation. *Int. J. Control* **43**, 741–766 (1986).
47. K. Zhou, J. C. Doyle, K. Glover, *Robust and Optimal Control* (Prentice-Hall Inc., 1996).
48. M. C. De Oliveira, J. Geromei, Linear output feedback controller design with joint selection of sensors and actuators. *IEEE Trans. Automat. Contr.* **45**, 2412–2419 (2000).
49. B. Boyacioglu, K. A. Morgansen, "Bioinspired observability analysis tools for deterministic systems with memory in flight applications," in *AIAA Scitech 2021 Forum* (Aerospace Research Central, 2021); https://doi.org/10.2514/6.2021-1679.
50. P. Sterling, S. Laughlin, *Principles of Neural Design* (MIT Press, 2015).
51. M. Verveld, Q. P. Chu, C. de Wagter, J. A. Mulder, "Optic flow based state estimation for an indoor micro air vehicle" in *AIAA Guidance, Navigation, and Control Conference* (American Institute of Aeronautics and Astronautics, 2010), pp. 2010–8209.
52. S. C. Whitehead, S. Leone, T. Lindsay, M. R. Meiselman, N. J. Cowan, M. H. Dickinson, N. Yapici, D. L. Stern, T. Shirangi, I. Cohen, Neuromuscular embodiment of feedback control elements in *Drosophila* flight. *Sci. Adv.* **8**, eabo7461 (2022).
53. H. G. Krapp, R. Hengstenberg, A fast stimulus procedure to determine local receptive field properties of motion-sensitive visual interneurons. *Vision Res.* **37**, 225–234 (1997).
54. K. Karmeier, R. Tabor, M. Egelhaaf, H. G. Krapp, Early visual experience and the receptive-field organization of optic flow processing interneurons in the fly motion pathway. *Vis. Neurosci.* **19**, 1–8 (2001).
55. N. Franceschini, "Sampling of the visual environment by the compound eye of the fly: Fundamentals and applications" in *Photoreceptor Optics* (Springer, 1975), pp. 98–125.
56. J. J. Koenderink, A. J. van Doorn, Facts on optic flow. *Biol. Cybern.* **56**, 247–254 (1997).
57. H. J. Dahmen, M. O. Franz, H. G. Krapp, "Extracting egomotion from optic flow: Limits of accuracy and neural matched filters" in *Motion Vision – Computational, Neural and Ecological Constraints*, J. M. Zanker, J. Zeil, Eds. (Springer, 2001), pp. 143–168.
58. M. O. Franz, J. S. Chahl, H. G. Krapp, Insect-inspired estimation of egomotion. *Neural Comput.* **16**, 2245–2260 (2004).
59. J. S. Humbert, R. M. Murray, M. H. Dickinson, "Sensorimotor convergence in visual navigation and flight control systems" in *Proceedings of the 16th IFAC World Congress* (International Federation of Automatic Control, 2005), pp. 253–258.
60. J. S. Humbert, A. Hyslop, Bio-inspired visuomotor convergence. *IEEE Trans. Robot.* **26**, 121–130 (2010).
61. A. Hyslop, J. S. Humbert, Autonomous navigation in three-dimensional urban environments using wide-field integration of optic flow. *J. Guid. Control Dynam.* **33**, 147–159 (2010).
62. R. Paul, A. Steiner, R. Gemperlein, Spectral sensitivity of *Calliphora erythrocephala* and other insect species studied with Fourier Interferometric Stimulation (FIS). *J. Comp. Physiol. A* **158**, 669–680 (1986).
63. S. M. Walker, A. L. R. Thomas, G. K. Taylor, Deformable wing kinematics in the desert locust: How and why do camber, twist and topography vary through the stroke? *J. R. Soc. Interface* **6**, 735–747 (2009).
64. C. Badrya, B. Govindarajan, J. D. Baeder, A. Harrington, C. M. Kroninger, Computational and experimental investigation of a flapping-wing micro air vehicle in hover. *J. Aircr.* **56**, 1610–1625 (2019).
65. C. Badrya, A. Sridharan, J. Baeder, C. Kroninger, Multi-fidelity coupled trim analysis of a flapping-wing micro air vehicle flight. *J. Aircr.* **54**, 10.2514/1.C034236 (2017).
66. K. MacFarlane, B. Bush, I. Faruque, J. Humbert, J. Baeder, "Quasi-steady and computational aerodynamics applied to hovering *Drosophila* dynamics" in *29th AIAA Applied Aerodynamic Conference* (Aerospace Research Central, 2011); https://doi.org/10.2514/6.2011-3793.
67. D. Paganin, S. C. Mayo, T. E. Gureyev, P. R. Miller, S. W. Wilkins, Simultaneous phase and amplitude extraction from a single defocused image of a homogeneous object. *J. Microsc.* **206**, 33–40 (2002).
68. J. Schindelin, I. Arganda-Carreras, E. Frise, V. Kaynig, M. Longair, T. Pietzsch, S. Preibisch, C. Rueden, S. Saalfeld, B. Schmid, J.-Y. Tinevez, D. J. White, V. Hartenstein, K. Eliceiri, P. Tomancak, A. Cardona, Fiji: An open-source platform for biological-image analysis. *Nat. Methods* **9**, 676–682 (2012).

69. M. Doube, M. M. Kłosowski, I. Arganda-Carreras, F. P. Cordelières, R. P. Dougherty, J. S. Jackson, B. Schmid, J. R. Hutchinson, S. J. Shefelbine, BoneJ: Free and extensible bone image analysis in ImageJ. *Bone* **47**, 1076–1079 (2010).
70. G. Taylor, Flight muscles and flight dynamics: Towards an integrative framework. *Anim. Biol.* **55**, 81–99 (2005).
71. I. Faruque, J. Sean Humbert, Dipteran insect flight dynamics. Part 1 longitudinal motion about hover. *J. Theor. Biol.* **264**, 538–552 (2010).
72. P. C. Müller, H. I. Weber, Analysis and optimization of certain qualities of controllability and observability for linear dynamical systems. *Automatica* **8**, 237–246 (1972).
73. G. E. Dullerud, F. G. Paganini, *A Course in Robust Control Theory: A Convex Approach* (Springer-Verlag, 2000).
74. H. Lee, Y. Park, Degree of controllability for linear unstable systems. *J. Vib. Control.* **22**, 1928–1934 (2016).
75. C. Kenney, G. Hewer, Necessary and sufficient conditions for balancing unstable systems. *IEEE Trans. Automat. Contr.* **32**, 157–160 (1987).
76. T. L. B. Flinois, A. S. Morgans, P. J. Schmid, Projection-free approximate balanced truncation of large unstable systems. *Phys. Rev. E* **92**, 023012 (2015).
77. A. Hać, L. Liu, Sensor and actuator location in motion control of flexible structures. *J. Sound Vib.* **167**, 239–261 (1993).
78. A. Singh, J. Hahn, Determining optimal sensor locations for state and parameter estimation for stable nonlinear systems. *Ind. Eng. Chem. Res.* **44**, 5645–5659 (2005).
79. H. R. Shaker, M. Tahavori, Optimal sensor and actuator location for unstable systems. *J. Vib. Control.* **19**, 1915–1920 (2013).
80. O. Kang, Y. Park, Y. S. Park, M. Suh, New measure representing degree of controllability for disturbance rejection. *J. Guid. Control Dynam.* **32**, 1658–1661 (2009).
81. H. Lee, Y. Park, "Degree of disturbance rejection capability for linear anti-stable systems" in *2014 14th International Conference on Control, Automation and Systems (ICCAS 2014)* (IEEE, 2014), pp. 154–156.
82. B. Marx, D. Koenig, D. Georges, "Optimal sensor and actuator location for descriptor systems using generalized Gramians and balanced realizations" in *Proceedings of the 2004 American Control Conference* (IEEE, 2004), vol. 3, pp. 2729–2734.
83. K. Manohar, J. Kutz, S. Brunton, Optimal sensor and actuator selection using balanced model reduction. *IEEE Trans. Automat. Contr.* **67**, 2108–2115 (2021).
84. J. Haag, A. Borst, Electrical coupling of lobula plate tangential cells to a heterolateral motion-sensitive neuron in the fly. *J. Neurosci.* **28**, 14435–14442 (2008).
85. J. Haag, A. Borst, Neural mechanism underlying complex receptive field properties of motion-sensitive interneurons. *Nat. Neurosci.* **7**, 628–634 (2007).
86. A. Borst, F. Weber, Neural action fields for optic flow based navigation: A simulation study of the fly lobula plate network. *PLOS ONE* **6**, e16303 (2011).

Acknowledgments: We thank Z. Turin, G. Gremillion, and J. Keshavan for discussions related to the dynamical systems formulation. We acknowledge the Paul Scherrer Institut, Villigen, Switzerland, for provision of synchrotron radiation beamtime at the TOMCAT beamline X02DA of the Swiss Light Source (SLS) and thank C. Schlepütz for assistance with synchrotron data collection. We thank R. Wehling, J. Evers, P. Bradshaw, and N. Rummelt for longstanding support of this research and for many conversations. We thank H. Cerbone, A. Yarger, B. Campbell, and J. Supple for comments. **Funding:** This work was sponsored by the US Air Force Research Laboratory (AFRL), the Air Force Office of Scientific Research (AFOSR), and the European Office of Aerospace Research and Development (EOARD) under AFOSR grant no. FA-9550-09-1-0075 to J.S.H.; EOARD contract no. FA8655-09-1-3083 to H.G.K; EOARD contract no. FA8655-13-1-3077 to G.K.T. and R.W.Z.; and AFOSR grant no. FA-9550-14-1-0068 to J.S.H., H.G.K., and G.K.T. This work was supported by Beamtime grant no. 20171617 to B.M. and G.K.T. from the Paul Scherrer Institute at the SLS, beamline TOMCAT. I.L.D. was supported by the Biotechnology and Biological Sciences Research Council, grant no. BB/M011224/1. S.M.W. and B.M. were supported by Royal Society University Research Fellowships. **Author contributions:** J.S.H., H.G.K., and G.K.T. conceived the presented idea with R.W.Z. H.G.K. conceived and supervised the electrophysiological experiments. J.V.H. developed the electrophysiology setup, and C.R. and Y.Y. carried out the recordings and analyzed the electrophysiological data. G.K.T. and S.M.W. conceived and supervised the wing kinematic measurements. I.L.D. and S.M.W. carried out the videogrammetric experiments and analysis, and I.N. and G.K.T. carried out the functional PC analysis. G.K.T. conducted the synchrotron experiments with B.M. and analyzed the tomographic data. J.D.B. supervised the CFD simulations. C.B., Y.S.J., and C.L. created and performed the simulations, and J.S.H., Y.S.J., and G.K.T. carried out the data analysis. J.S.H. and G.K.T. developed the theoretical framework. J.S.H., A.H., A.L., and G.K.T. conceived and performed the dynamical systems analysis. J.S.H. and G.K.T. wrote the manuscript with H.G.K. All authors participated in reviewing the manuscript. **Competing interests:** The authors declare that they have no competing interests. **Data, code, and materials availability:** The data and code that support the findings of this study are available in Zenodo with the identifier doi:10.5281/zenodo.18601858. All reagents and materials associated with this study are listed in the Materials and Methods section and/or are available commercially.

Submitted 26 March 2025
Accepted 12 February 2026
Published 11 March 2026
10.1126/scirobotics.adx7524

Science Robotics

Fly motion vision maximizes signal energy transfer between mechanical input and sensor output

J. Sean Humbert, Holger G. Krapp, James D. Baeder, Camli Badrya, Inés L. Dawson, Jiaqi V. Huang, Andrew Hyslop, Yong Su Jung, Alix Leroy, Cosima Lutkus, Beth Mortimer, Indira Nagesh, Clément Ruah, Simon M. Walker, Yingjie Yang, Rafal W. #bikowski, and Graham K. Taylor

Sci. Robot. **11** (112), eadx7524. DOI: 10.1126/scirobotics.adx7524

Science Robotics (ISSN 2470-9476) is published by the American Association for the Advancement of Science. 1200 New York Avenue NW, Washington, DC 20005. The title *Science Robotics* is a registered trademark of AAAS.